SPH-DEM Modeling of the Seismic Response of Shallow Foundations Resting on Liquefiable Sand

Saman Farzi Sizkow[1], Usama El Shamy[2]

January 28, 2022

[1]Graduate Research Assistant, Civil and Environmental Engineering Dept., Southern Methodist University, PO Box 750340, Dallas, TX 75275, E-mail: sfarzisizkow@smu.edu

[2]Associate Professor, Civil and Environmental Engineering Dept., Southern Methodist University, PO Box 750340, Dallas, TX 75275, E-mail: uelshamy@lyle.smu.edu (Corresponding author)

Abstract

In this study, the seismic response of shallow foundations resting on a liquefiable soil layer is modeled using a coupled smoothed particle hydrodynamics (SPH)-discrete element method (DEM) scheme. In this framework, the soil deposit is represented by an assembly of DEM particles and the fluid domain is lumped into a set of SPH particles carrying local fluid properties. The averaged forms of Navier-Stokes equations dictate the motion of the fluid-particle mixture and the interphase forces are estimated using well-known semi-empirical equations. A saturated soil-foundation system with an average contact pressure of 50 kPa was created using the coupled scheme. The foundation block was composed of a collection of DEM particles glued

together by high-stiffness bonds. No-penetration boundary condition was applied to all sides of the foundation block to allow for fluid-foundation interaction. The model was subjected to a strong base acceleration and the response was analyzed and compared to the free-field. The ground settlement in the soil-foundation system mostly originated from co-seismic deviatoric deformations while volumetric strains were the main contributing factor at the free-field. In addition, the impact of soil permeability on the seismic response of the soil-foundation system was examined by changing the pore fluid viscosity. According to the results, as the soil permeability decreased, smaller excess pore pressures developed beneath the footing thanks to the slower migration of pore fluid from the sides and bottom, and a larger magnitude of soil strength and stiffness was maintained in the expansive zone. As a result, the system with the lowest permeability experienced the smallest foundation settlement while the foundation acceleration amplitude was the highest in this case. The results also showed that the percentage of post-shaking settlement appreciably increased in the lower-permeability deposits. The results of this study were compared with the published centrifuge studies that showed good qualitative consistency.

1 INTRODUCTION

Saturated loose sand can experience significant excess pore pressure buildup and accompanying stiffness and strength degradation during strong seismic events. Structures founded on such soils may sustain excessive tilting and settlement due to loss of foundation soil bearing capacity and accumulation of dynamic deformations. Liquefaction-inflicted building failures were reported during several major earthquakes, including the 1964 Niigata earthquake [1, 2], the 1990 Luzon earthquake [3, 4], the 1999 Izmit earthquake [5], the 2010 Chile earthquake [6], the 2011 Tohoku earthquake

[7], and the 2010-2011 Christchurch earthquake [8]. The mechanism behind the dynamic settlement of shallow foundations supported by a liquefiable stratum is quite complex. However, the currently accepted engineering practices for assessing liquefaction-induced settlement beneath shallow foundations generally follow the same procedures developed for free-field conditions [9, 10]. These methods can lead to highly inaccurate estimations, as in the presence of a superstructure, the problem can no longer be treated as a one-dimensional case and 3D analysis is needed. The static surcharge imposed by the structure and the dynamic interaction between the footing and the underlying soil produce shear stresses and deformations within the foundation soil that could drastically change the pore pressure buildup patterns and the settlement mechanisms. In fact, it has been shown that in contrast to the free-field settlement, where the key process is the volumetric strains stemming from reconsolidation of the liquefied layer, in soil-shallow foundation systems, both co-seismic deviatoric strains and post-seismic volumetric strains contribute to the overall settlement, with the former being more dominant [11].

To gain a deeper insight into the complicated settlement mechanism of shallow foundations on liquefiable soils, physical modeling including 1-g shaking table tests and centrifuge studies (e.g., [2, 11–22]) are being widely utilized alongside the field investigations and the available data from the case histories. Yoshimi and Tokimatsu [2] conducted a series of shaking table tests to investigate the influence of different parameters on the dynamic settlement of a model structure founded on liquefiable soil. The studied parameters were contact pressure, excess pore pressure buildup, soil density and structure width. Liu and Dobry [12] performed centrifuge modeling to study the effectiveness of sand densification in reducing liquefaction-induced settlement of shallow foundations. They also used a range of fluid viscosities in their models to reveal the impact of soil permeability on the response. Adalier et al. [13] studied the seismic response of shallow foundations resting on non-plastic silty soils through centrifuge tests. In addition, stone columns were installed in the models as a countermeasure against liquefaction and the results were reported. Centrifuge experiments were performed by Dashti et al. [14] to discover the key factors contributing to the settlement of shallow foundations on liquefiable ground. Different remediation techniques were also employed, and their effectiveness was discussed. Zeybek and Madabhushi [23] investigated the effect of air-injection, as a liquefaction remediation technique, on the settlement mechanism of shallow foundations.

This subject has also been explored through numerical modeling in numerous studies (e.g., [24–40]). Most of these works employ continuum techniques such as the finite element method (FEM) and the finite difference method (FDM). These macroscale approaches to mimicking complicated soil behavior require intricate constitutive laws that usually involve a large set of calibration parameters. Popescu and Prevost [24] developed a FEM-based numerical scheme for soil liquefaction. Their multiyield plasticity model required several constitutive soil parameters, namely state parameters, low-strain elastic parameters, dilation parameters, and yield parameters. Elgamal et al. [25] used 3D FEM simulations to investigate soil liquefaction and associated settlements under a superstructure. They also explored different mitigation measures such as soil compaction and increasing the soil permeability below the foundation. Popescu et al. [26] developed a nonlinear extension of Biots theory. They implemented the proposed scheme in a FEM framework and applied it to the study of seismic settlement of structures founded on liquefiable ground. Karamitros et al. [30] used nonlinear FDM to study the response of a saturated soil-foundation system. The focus of their work was on excess pore pressure buildup under the foundation, seismic foundation settlement, degradation of bearing capacity, and soil-structure interaction. Karimi and Dashti [31] employed centrifuge modeling and nonlinear FEM analysis to study the dynamic soil-foundation interaction on liquefiable ground. They investigated foundation acceleration, settlement, tilt, and maximum drift through numerical simulations.

In view of the discrete element method (DEM) proven capabilities in reproducing nonlinear soil behavior through microscale modeling of individual soil grains and capturing complex soil-structure interaction by direct tracking of contact forces, many researchers have strived to couple DEM with various computational fluid dynamics (CFD) techniques to extend its applicability to simulations involving saturated soil. Two of the most popular coupled schemes that incorporate DEM are the continuum-discrete methods (e.g., [41–48]) and the pore-scale techniques (e.g., [49–64]). Sun et al. [65] coupled DEM with smoothed particle hydrodynamics (SPH) to simulate particle-fluid mixtures. In this method, the soil is modeled by DEM particles and the fluid domain is represented in SPH as a set of lumped masses that hold local fluid properties. Averaged forms of Navier-Stokes equations are discretized using SPH particle summation and numerically solved to track the fluid motion. Well-established semi-empirical relations describe the interaction forces between the two phases. Numerous studies have been conducted in different disciplines of science and engineering using this coupled scheme (e.g., [66–75]). Compared to the fully continuum-based methods, apart from the inherent benefits of DEM, this coupled scheme is capable of successfully capturing complicated phenomena related to seismic response of saturated geotechnical systems such as pore water pressure generation, degradation of soil strength and stiffness, deamplification of input motion in liquefied layers, simultaneous soil-fluid-structure interaction, and regain in soil strength due to dilative soil behavior without the need for a sophisticated constitutive model, special interface elements, or many simplifying assumptions [73–75]. The familiar trends captured by the coupled SPH-DEM method are, unlike the continuum-based techniques, direct results of micromechanical mechanisms such as local volumetric strain due to rearrangement of soil particles, changes in the average number of contacts between soil particles, and mutual interactions between soil grains, structure, and fluid. Compared to the continuum-discrete techniques (in which the fluid domain is discretized into large fixed cells), it can handle much more complicated model geometries, as the SPH particles can be placed in different configurations to fit the model requirements. In addition, the presence of shallow foundation requires moving impermeable boundary conditions that pose a big challenge for the fixed-mesh techniques. Finally, compared to the pore-scale methods such as LBM-DEM, it is computationally far less demanding while displaying comparable accuracy [76]. The main drawback of this technique is the fact that the fluid is assumed to be weakly compressible, which can be compensated for by using a large enough numerical speed of sound that limits the density fluctuations to very small values.

The authors previously utilized the above-mentioned SPH-DEM method to analyze geotechnical problems involving soil liquefaction and large deformations, which showed qualitative consistency with published experimental studies [73–75, 77]. In this paper, the ability of this coupled scheme to model the seismic response of shallow foundations resting on liquefiable soil is examined. This study aims to assess its potential in analyzing soil-fluid-structure interaction by qualitatively comparing the results with the observations reported in published centrifuge studies. The saturated soil layer was created using DEM and SPH particles. The foundation was modeled by a collection of DEM particles that were glued together by high-stiffness parallel bonds to act as a single rigid block. A model with average footing contact pressure of 50 kPa was created and subjected to a strong seismic base excitation. Different aspects of the response such as excess pore pressure buildup, soil deformation, average particle acceleration, degradation of soil strength and stiffness, foundation settlement, and dynamic soil-footing interaction were evaluated. Moreover, the viscosity of the pore fluid was changed to analyze the effect of soil permeability on the seismic response of soil-foundation systems.

2 COUPLED SPH-DEM SCHEME

In the proposed coupled scheme, SPH was employed to solve the equations of fluid motion. In SPH, the fluid domain is replaced by a set of discrete particles holding local fluid properties such as density and pressure [78]. The average forms of continuity and momentum equations were discretized through interpolation of various quantities over the influence domain of any given particle. The equation of state for weakly compressible fluid was utilized to evaluate the fluid pressure based on the local density. In addition, negligible density fluctuations were ensured by setting the numerical speed of sound to a proper value. Soil particles were modeled by rigid spherical particles in DEM with rolling friction between them to limit their unrealistic relative rotations. The coupling forces between the soil and fluid were also quantified using well-established semi-empirical relations, in which the interactions are calculated based on the local porosity and relative velocities between the two phases. The DEM cycles were performed using the PFC3D software [79] and the SPH part of the coupled scheme was implemented using a user-written Cython code and linked to the PFC3D environment. The fluid and solid phase equations were solved using explicit time integration schemes. A constant value was selected for the DEM timestep. The SPH timestep was assumed to be N times the DEM timestep, where N is an integer. This means that N DEM computation cycles should be performed per one SPH cycle. The first step in a single SPH-DEM computational loop is to calculate the fluid particle properties such as porosity and pressure. The interaction forces are next obtained based on the latest positions and velocities of DEM particles, and the interpolated porosities at their locations. Then the SPH particle densities, velocities and positions are updated according to the variation rates of density and velocity computed from their pressure, superficial density and the coupling forces. Finally, the interaction forces are applied to the solid particles and N DEM cycles are performed to get the updated particle positions and velocities. The new positions and velocities are then sent as inputs to the SPH algorithm and the next loop begins. A schematic view of the SPH-DEM model is presented in Fig. 1.

Due to some major issues, it was not possible to conduct a one-to-one comparison with published centrifuge studies on the response of shallow foundations resting on liquefiable soils. Some of these difficulties were: 1) The dissipation phase in the centrifuge studies usually takes several minutes or longer due to relatively low soil permeability. Conducting a similar experiment using the presented coupled scheme on a desktop computer would lead to impractical simulation times. 2) The model setup in the centrifuge tests requires the lateral boundaries to be placed far away from the foundation block in order to represent the free-field conditions. Such large models would need a huge number of DEM particles to simulate and the computational costs would be immense. 3) In most centrifuge studies, the dynamic soil properties are not fully described which makes it very difficult to create a relatively accurate numerical model of the real soil deposit. In view of these difficulties, a building block approach was adopted by the authors to validate the proposed coupled SPH-DEM model [73, 74]. The main coupling parameters between the fluid and particles in this model stem from porosity calculation, averaged solid particle velocities and the resulting drag force. Therefore, a simulation was performed to examine the ability of the model to correctly predict the drag force on a few settling particles in a fluid column [73]. Since this system has a diluted concentration of particles, it presents an extreme in computing porosity and associated drag forces. It also includes the challenge of large solid particle velocities. Additionally, another extreme situation in which flow in a dense stagnant arrangement of a porous medium was considered to examine the ability of the fluid code to accurately predict fluid velocities in such a dense packing [74]. More validation cases for the coupled SPH-DEM scheme can be found in Wu et al. [72], He et al. [80], Wu et al. [81]. A description of the model components are provided in the following sections.

2.1 Fluid phase

The motion of solid-fluid mixture is governed by the averaged forms of Navier-Stokes equations as described by Robinson et al. [82]:

$$\frac{\partial(n\rho_f)}{\partial t} + \nabla.(n\rho_f \mathbf{u}) = 0 \tag{1}$$

$$\frac{\partial(n\rho_f \mathbf{u})}{\partial t} + \nabla.(n\rho_f \mathbf{u}\mathbf{u}) = -\nabla P + \nabla.\boldsymbol{\tau} + n\rho_f \mathbf{g} - \mathbf{f^{int}} \tag{2}$$

in which ρ_f is the fluid density, n is the porosity, P is the fluid pressure, $\boldsymbol{\tau}$ is the viscous stress tensor, $\mathbf{f^{int}}$ is the fluid particle interaction force, $\mathbf{g}$ is the gravitational acceleration vector and $\mathbf{u}$ is the fluid velocity. To avoid confusion, hereafter, the subscripts i and j are used for the SPH particles and a and b indicate the DEM particles. In this study the Wendland kernel function is chosen as the smoothing function [83]:

$$\begin{cases} W(|\mathbf{r}|, h) = \alpha_D (1 - \frac{q}{2})^4 (1 + 2q) & 0 \leq q \leq 2 \\ 0 & 2 < q \end{cases} \tag{3}$$

in which $q = \frac{|\mathbf{r}|}{h}$ and $\alpha_D = \frac{21}{16\pi h^3}$. Applying SPH particle summation, Eqs. 1 and 2 can be rewritten as:

$$\begin{aligned} \frac{d(n_i\rho_i)}{dt} &= \sum_j m_j \mathbf{u_{ij}}.\nabla_i W(|\mathbf{r_{ij}}|, h) && (4) \\ \frac{d\mathbf{u_i}}{dt} &= -\sum_j m_j [\frac{P_i}{(n_i\rho_i)^2} + \frac{P_j}{(n_j\rho_j)^2} + R_{ij}(\frac{W(|\mathbf{r_{ij}}|, h)}{W(\Delta p, h)})^4]\nabla_i W(|\mathbf{r_{ij}}|, h) + \mathbf{\Pi}_{ij} + \frac{\mathbf{f^{int}}}{m_i} + \mathbf{g} && (5) \end{aligned}$$

with $\mathbf{u_{ij}}$ being the relative velocity vector, P_i fluid pressure evaluated at the location of particle i, R_{ij} the tensile instability term to prevent particles from forming small clumps and $\mathbf{\Pi}_{ij}$ the viscosity term. R_{ij} and $\mathbf{\Pi}_{ij}$ are defined as [84, 85]:

$$\begin{aligned} \mathbf{\Pi}_{ij} &= \sum_j \frac{m_j(\mu_i + \mu_j)\mathbf{r_{ij}}.\nabla_i W(|\mathbf{r_{ij}}|, h)}{\rho_i\rho_j(|\mathbf{r_{ij}}|^2 + 0.01h^2)}\mathbf{u_{ij}} && (6) \\ R_{ij} &= \begin{cases} 0.01[\frac{P_i}{(n_i\rho_i)^2} + \frac{P_j}{(n_j\rho_j)^2}] & P_i > 0 \textit{ and } P_j > 0 \\ 0.2[\left|\frac{P_i}{(n_i\rho_i)^2}\right| + \left|\frac{P_j}{(n_j\rho_j)^2}\right|] & \textit{otherwise} \end{cases} && (7) \end{aligned}$$

The porosity at the position of a fluid particles can be estimated by particle summation over all DEM particles present within its kernel radius:

$$n_i = 1 - \sum_a W(|\mathbf{r_{ai}}|, h)V_a \qquad (8)$$

in which $|\mathbf{r_{ai}}|$ is the distance between fluid particle i and DEM particle a and V_a is the volume of the DEM particle. The weakly compressible equation of state is used to calculate the fluid pressure.

This equation provides a relationship between the fluid pressure and its density [86]:

$$P_i = \frac{\rho_0 {c_s}^2}{\gamma}((\frac{\rho_i}{\rho_0})^\gamma - 1) \tag{9}$$

where ρ_0 is the reference density, c_s is the numerical sound speed, and γ is usually set to 7. The numerical speed of sound is usually considered to be 10 times higher than the maximum fluid velocity to limit the fluctuations of the fluid density to less than 1% of its initial value [86].

In this paper, the solid boundaries for SPH particles are treated in the same manner as described by Adami et al. [87]. In this approach, the solid boundary is represented by two layers of dummy particles. These particles compensate for the domain truncation near the boundary and provide kernel support for the adjacent fluid particles. To ensure no-slip boundary condition the velocities of the dummy particles are extrapolated from the surrounding fluid particles:

$$\mathbf{u_w} = 2\mathbf{u_0} - \tilde{\mathbf{u}}_\mathbf{w} \tag{10}$$

$$\tilde{\mathbf{u}}_\mathbf{w} = \frac{\sum_j \mathbf{u_j} W(\left|\mathbf{r_{wj}}\right|, h)}{\sum_j W(\left|\mathbf{r_{wj}}\right|, h)} \tag{11}$$

in which $\mathbf{u_0}$ is the prescribed wall velocity. In addition, in order for the dummy particles to produce correct pressure gradient near the boundary, the pressure and density of wall particles should also be calculated from the neighboring fluid particles:

$$P_w = \frac{\sum_j P_j W(\left|\mathbf{r_{wj}}\right|, h) + (\mathbf{g} - \mathbf{a_w}).\sum_j \rho_j \mathbf{r_{wj}} W(\left|\mathbf{r_{wj}}\right|, h)}{\sum_j W(\left|\mathbf{r_{wj}}\right|, h)} \tag{12}$$

$$\rho_w = \rho_0(\frac{P_w}{B} + 1)^{\frac{1}{\gamma}} \tag{13}$$

Periodic boundaries represent a condition where the domain is extended infinitely on the sides. The implementation of this type of boundary condition is rather straightforward in SPH. In this case, the two sides of the model are considered adjacent to each other and, therefore, the truncated support domain of a particle close to one side is completed by contributing particles on the opposite side. In addition, if a particle crosses a periodic boundary it will re-enter the domain from the other side with the same velocity.

2.2 Particulate phase

In the linear contact model, the interaction of DEM particles is described by a set of normal and shear springs and dashpots. The relative particle movements produce normal and shear elastic forces in the springs, and the viscous behavior is provided by the dashpots. In granular systems, the energy dissipates through various micro-mechanical processes, such as contact adhesion, surface roughness and particle non-sphericity [79]. When the soil grains are idealized as spherical DEM particles, the effects of particle shape on the energy loss during relative rotation of particles, can be compensated for by addition of rolling friction between particles [88–91]. In this study, the rolling resistance contact model is utilized which is similar to the linear contact model, but with the difference that the relative rotation of particles generates a moment that resists their motion and acts as an energy dissipation mechanism [79]. It should be noted that, in general, energy dissipation in DEM stems mainly from inter-particle sliding-induced friction as particles slide, which is accounted for in the simulations [92]. In this sense, material damping is inherently accounted for in the simulations and its actual magnitude depends on the level of sliding between contacts.

2.3 Fluid-particle interaction

The force applied by the fluid on the DEM particle a can be resolved into the drag force ($\mathbf{F_a^D}$) and pressure gradient force ($\mathbf{F_a^P}$) [93]:

$$\mathbf{F_a^{int}} = \mathbf{F_a^D} + \mathbf{F_a^P} \tag{14}$$

The semi-empirical relation proposed by Ergun [94] is used to estimate the fluid drag force based on the local porosity and the relative velocity between the two phases:

$$\mathbf{F_a^D} = \frac{\beta V_a}{1-n_a}(\mathbf{\bar{u}_a} - \mathbf{u_a}) \tag{15}$$

where $\mathbf{\bar{u}_a}$ is the average local fluid velocity, $\mathbf{u_a}$ is the solid particle velocity, V_a is the solid particle volume, β is the interphase momentum exchange coefficient and n_a is the average local porosity. β can be obtained from two separate relations based on the local porosity [94]:

$$\beta = \begin{cases} 150\frac{(1-n_a)^2}{n_a}\frac{\mu}{d_a^2} + 1.75(1-n_a)\frac{\rho}{d_a}\left|\mathbf{\bar{u}_a} - \mathbf{u_a}\right| & n_a \leq 0.8 \\ 0.75C_d\frac{n_a(1-n_a)}{d_a}\rho\left|\mathbf{\bar{u}_a} - \mathbf{u_a}\right| n_a^{-2.65} & n_a > 0.8 \end{cases} \tag{16}$$

in which μ is the dynamic viscosity of the fluid, d_a is the solid particle diameter and C_d is the drag coefficient given by:

$$C_d = \begin{cases} \frac{24}{Re_a}(1+0.15Re_a^{0.687}) & Re_a \leq 1000 \\ 0.44 & Re_a > 1000 \end{cases} \tag{17}$$

Re_a is the particle Reynolds number that can be calculated from [95]:

$$Re_a = \frac{|\bar{\mathbf{u}}_\mathbf{a} - \mathbf{u}_\mathbf{a}| n_a \rho d_a}{\mu} \tag{18}$$

The fluid particle i will also receive reaction forces from all DEM particles within its support domain:

$$\mathbf{f}_\mathbf{i}^\mathbf{int} = -\frac{m_i}{\rho_i} \sum_a \frac{W(|\mathbf{r}_\mathbf{ai}|, h)}{\sum_j \frac{m_j}{\rho_j} W(|\mathbf{r}_\mathbf{aj}|, h)} \mathbf{F}_\mathbf{a}^\mathbf{int} \tag{19}$$

3 Computational Models

A soil-foundation system with an average footing pressure of 50 kPa was created utilizing the described coupled SPH-DEM scheme and used in the numerical simulations. The same saturated deposit without the foundation was used to simulate the free-field conditions. The soil-foundation model was meant to represent an isolated square footing along with its supporting soil in a group of footings. Figure 2 shows the assumed arrangement of the square footings in a liquefaction-prone site. The foundation blocks were 0.8 m thick, 3 m$\times$3 m in lateral dimensions, and equally spaced at center-to-center distances of 7 m. The soil deposit was assumed to be a 4.25-m saturated sand layer underlain by a bedrock. Since a repeated pattern can be detected in this setup (Fig. 2), only a small area enclosing a single footing (shown with dashed lines) was selected and periodic boundary conditions were applied to its lateral sides. These boundaries simulate a condition where the model is periodically repeated on its sides, as can be seen in this case. A rigid wall was placed at the bottom of the domain to represent the bedrock. Similar to centrifuge experiments, a high gravitational field of 50g was employed in the numerical simulations to downscale the prototype to a practical size. This way, the number of DEM particles can be drastically reduced, as the centrifuge scaling laws dictate that the model dimensions must be scaled down by a factor of 50 under this strong gravitational acceleration. This means that the footing and soil deposit dimensions were reduced to 6 cm$\times$6 cm$\times$1.6 cm and 14 cm$\times$14 cm$\times$8.5 cm, respectively. The values presented in this study are exclusively in prototype units unless otherwise specified. Note that the employed high gravitational field and associated high stresses do not cause particle crushing and therefore the grains remain essentially spherical. Further, since the objective of this study is liquefaction, only dynamic time scaling is observed and not consolidation time scaling as typically done in centrifuge testing.

DEM particles with sizes ranging from 1.5 mm to 2.5 mm (similar to grain sizes of coarse sand) were selected for the conducted simulations. Note that, due to computational limitations, the ratio of foundation width to the average grain size in the deposit was about 30 which is slightly less than the limit of 35 recommended in centrifuge testing of shallow foundation to minimize the effect of the number of particles at the interface between soil and foundation on the response of the system [96]. To create the soil deposit, first, the approximate number of particles were calculated based on the average particle size, the model volume, and the desired porosity. Then they were generated in a relatively large space and released to settle under the gravitational force. The average porosity and the saturated unit weight of the final deposit were determined to be approximately 0.43 and 19 $\mathrm{kN/m^3}$, respectively. SPH particles with spacing and smoothing length (h) of, respectively, 4 mm and 6 mm were introduced into the domain to fully saturate the deposit. Periodic boundary conditions were also enforced at the lateral sides of the fluid domain. A no-slip no-penetration boundary layer was created at the bottom of the model, where the bedrock was located. Due to the high gravitational field of 50g and the relatively large particle sizes used in this study, a fluid with a much higher viscosity compared to water was employed so that the permeability of the assembly of particles would fall within the acceptable range for sands. The prototype fluid viscosity was initially set to 0.02 Pa.s (1.0 Pa.s in model units). According to the Kozeny-Carmen equation and based on the model properties, the initial soil permeability was estimated to be around 3 mm/s (same order of coarse sand) [97]. The shallow foundation consisted of DEM particles that were glued together by very high-stiffness parallel bonds [79] to simulate a rigid block. Clumped particles could more accurately represent a rigid body, however, due to some implementation difficulties associated with tracking of individual pebbles constituting a clump, parallel bonds were used instead in this study. The density of foundation particles was adjusted so that the footing would impose the target pressure of 50 kPa. In order to make all sides of the foundation block impermeable to fluid, SPH particles were placed at the position of DEM particles constituting the blocks surface. Each pair of these co-located SPH and DEM particles acts as a single hybrid particle that receives hydrodynamic forces from the surrounding SPH particles and interacts with the DEM particles at the contact points. This method is commonly used in fluid-structure interaction problems using SPH [72]. The footing was placed on the soil layer surface and the model was allowed to reach equilibrium. A 3D view of the modeled soil-shallow foundation system and a summary of the parameters used in the DEM simulations are provided in Fig. 3 and Table 1, respectively.

Prior to performing the main simulations, it was necessary to obtain the soil mechanical and dynamic properties. Therefore, a numerical drained triaxial test was first performed on a sample with the same microscale properties and packing density as the main deposit, and the soil friction angle was found to be around 30 degrees. According to the general bearing capacity equation [98], the ultimate static bearing capacity of the shallow foundation neglecting neighboring footings effects was approximately 185 kPa, which yields a static safety factor of 3.7. The saturated deposit was then excited with a small acceleration amplitude of 10^{-3}g and the cyclic shear stress-strain loops were plotted to obtain the low strain shear modulus, which was approximately 25.2 MPa. The level of strains induced by this weak excitation was very low and, therefore, the soil stress-strain behavior was almost perfectly linear. The shear wave velocity and the fundamental frequency of the deposit were calculated based on the low strain shear modulus and determined to be around 114 m/s and 6.7 Hz, respectively.

4 Computational Simulations

A seismic signal with a maximum amplitude of 0.25g and a frequency of 3 Hz was introduced into the models through the bedrock. The input acceleration followed a sinusoidal pattern in which the amplitude linearly increases to reach its maximum during the first 3 seconds. It then remains constant for the next 4 seconds (from 3 s to 7 s) and finally, it linearly decreases to zero in the last second (from 7 s to 8 s). Different quantities were recorded throughout the simulations, such as excess pore pressure, average particle acceleration, coordination number, stress and strain tensors, forces exerted on the foundation by the soil and fluid, and foundation acceleration and settlement. The data was collected within measurement volumes distributed over a plane parallel to the shaking direction and crossing the models center. The location of the measurement volumes are illustrated in Fig. 4. In this section, first, the seismic response of the saturated deposit overlain by the foundation is examined and compared to the free-field. Then different aspects of the foundation response are investigated. Finally, the effect of soil permeability on the behavior of the soil-foundation system is analyzed.

4.1 Response of saturated deposits

Figure 5 shows the time histories of excess pore pressure ratio (EPPR), which was defined as the ratio of excess pore pressure to the initial vertical effective stress, during the simulations at different locations. In the free-field model, the evolution of EPPR seems to be almost identical at locations with the same depth. It developed faster near the surface layers and the value of one, which is indicative of liquefaction, was reached in almost the entire deposit. The observed trends were different for the deposit overlain by the foundation. It can be noticed that EPPR was generally much lower than the free-field model, especially below the foundation center (locations 9-12). In addition, contrary to the free-field case, EPPR decreases moving toward the surface at locations 5-8 and 9-12, suggesting that the foundation had a favorable effect in reducing the liquefaction susceptibility in their adjacent regions. The trend is reversed at locations 1-4, where similar to the free-field, the maximum EPPR increases moving upward and values close to one were reached at the top layer (depth of 1 m). The response at locations 1-4 between the footings, however, is not quite the same as the free-field. This outcome was expected as a lateral distance of 2B (B is the footing width which in this case is 3 m) from the footing center is generally required so that free-field conditions can be assumed [11, 99]. Locations 1-4 have a horizontal distance of 3 m from the centerline and, therefore, their responses were still affected by the foundations. Smaller or even negative EPPR underneath the footings was reported in many centrifuge studies (e.g., [12, 13, 18]). The profiles of excess pore pressure in the free-field and the soil-foundation system are presented in Fig. 6. According to this figure, the top 2.5 m of the free-field model liquefied during the seismic loading (Fig. 6a). Liquefaction first took place near the surface and then it propagated toward the model base. However, dissipation of excess pore pressure started from the base and then it happened in the upper layers. In the soil-foundation system, only the surface layers (top 1.5 m) near the model lateral boundary liquefied (Fig. 6b) and at locations close to the footing (Fig. 6c and d), the excess pore pressure was significantly smaller than the initial effective stress.

The foundation reduces the liquefaction potential of the supporting soil in two major ways: (1) by increasing the initial effective stresses, and (2) by inducing dilative response in the underlying soil. Figure 7 shows the accumulation of volumetric strain at different locations throughout the deposits. According to this figure, negative volumetric strains or, in other words, contraction of pore spaces occurred in the entire free-field sand layer that resulted in large excess pore pressure buildup and full liquefaction of the deposit. In the soil-foundation system, however, development of positive volumetric strains under the footing is evident, signifying soil dilative behavior. This expansion of pore spaces is partly responsible for the considerably lower EPPR beneath the footing compared to the free-field. Moving horizontally or vertically away from the footing, the dilative response becomes less pronounced. The contours of maximum EPPR reached during the entire course of each simulation and the total volumetric strain are provided in Fig. 8. The two sets of contours are consistent in that EPPR was much lower inside the expansive zone below the foundation compared to the sides where the volumetric strain was mostly negative. As discussed earlier, no signs of dilation can be detected within the free-field model and the entire deposit liquefied.

The dilative response of the foundation soil arises from soil shearing due to footing-induced static shear stresses and lateral outflow of soil grains [12, 13]. Figure 9 shows the contours of maximum static shear stress at the start of the soil-foundation simulation. In order to obtain these contours, the stress tensors were recorded inside a large number of measurement spheres throughout the deposit. Then the principal stresses were calculated using eigenvalue analysis at each location and the maximum shear stresses were subsequently obtained. A circular area of high intensity can be detected below the footing. Going down from the surface, the magnitude of maximum shear stress decreases while the influence domain almost linearly expands.

Figure 10 shows the contours of shear strain at different time instants during the seismic loading. According to these contours, no significant shear strain developed during the first 3 seconds of shaking. Around the 5 s mark, shear strain started to accumulate mostly below the foundation edges and its magnitude gradually increased until the end of shaking (8 s). It is also evident from this figure that the accumulated shear strains at the two sides of the model had similar magnitudes but opposite signs. These contours are consistent with the shear strain contours presented by Adamidis and Madabhushi [19], and Macedo and Bray [34]. The contours of horizontal, vertical and total displacements at the end of simulations are presented in Fig. 11. In the free-field model, the particle displacements were mostly vertical and the horizontal component was negligible. This means that most of the deformation was volumetric and the deviatoric part was insignificant. In addition, larger deformations took place in the shallow layers that reduced to almost zero at the model base. The contours look very different for the soil-foundation system. The horizontal displacement contours show large deformations below the footings edges (Fig. 11b). The particles motion on the left and right sides seems symmetrical and away from the centerline. The maximum vertical displacement was located directly below the footing with a maximum value of more than 40 cm (Fig. 11a). A ground upheaval of higher than 10 cm can also be noticed at both sides of the model. It can be deduced from the results that the deviatoric deformation was the governing mechanism behind ground settlement in the case of soil-foundation system as the volumetric strains below the foundation were mostly positive (Fig. 8b). These contours are consistent with the patterns presented in the published studies by Zeybek and Madabhushi [17], and Adamidis and Madabhushi [19]. The deformation mechanism in the soil-foundation model can be better seen in

Fig. 12. Three zones were detected based on the deformation patterns at various locations. In a triangular-shaped area directly below the foundation, generally larger deformations occurred which were almost completely vertical toward the base. The displacement patterns were, however, quite different in the regions on the two sides of the foundation, in which the soil particles moved to the sides and upward toward the surface. These patterns can be explained by the fact that as the foundation soil settled, it pushed the weaker surrounding soil away (the confining pressure was lower in these areas due to pore pressure buildup) and caused the ground surface to heave on both sides. This mechanism is similar to the one proposed by Adamidis and Madabhushi [19] for a foundation resting on a shallow soil layer. The difference between the two mechanisms, especially near the lateral boundaries, is due to the fact that the model analyzed by Adamidis and Madabhushi [19] consisted of an isolated foundation, but in this study, the response of a single foundation in a group of foundations was investigated and, therefore, free-field conditions cannot be assumed for the lateral sides of the model. Figure 13 demonstrates side views of the initial and final deformed shapes of the models. Particles were colored in black and white to form horizontal and vertical lines in order to better visualize the deformation mechanisms at various locations. In the case of soil-foundation model, the concentration of shear strain under the footing edges is evident from the distortion and rotation of the small square elements. For the free-field model, contrary to the soil-foundation system, the overall shape of the square elements seems to have been maintained.

The time histories of ground settlement at the models center and near the left boundary of the models are presented in Fig. 14. In the deposit with the foundation, the settlement started to accumulate almost linearly after the first few seconds and continued until the end of loading. The results show that the amount of ground settlement below the foundation was slightly higher than 40 cm. This value is significantly larger than what is accepted in the design of shallow foundations that limits the maximum settlement to 25 mm [98]. This indicates that while the foundation soil did not reach full liquefaction marked by an EPPR of 1.0, there was enough stiffness degradation that led to large deformations. The ground heave (around 10 cm) can also be seen at the boundary location away from the footing. In the free-field model, the settlement histories look similar at the two locations. The total surface settlement in this case is significantly lower than the other deposit at approximately 5 cm. It is also worth mentioning that a relatively large magnitude (31%) of free-field settlement happened post-shaking due to soil reconsolidation. This is contrary to the soil-foundation system in which almost the entire settlement occurred during seismic loading. These observations are in agreement with the results of reported centrifuge studies (e.g., [13]).

Figure 15 demonstrates the time histories of average particle acceleration at different locations inside the free-field model and the soil-light foundation system. A significant decay of acceleration after the first 3 seconds of loading (around the onset of liquefaction) is visible at all depths of the free-field model. This attenuation of input motion was much more pronounced in the shallow layers where it almost completely vanished (Fig. 15a). Figure 15b shows a different trend for the deposit with the foundation. The reduction in the acceleration amplitude was far less significant compared to the free-field, especially under the footing center (locations 9-12). At location 5, which is located below the footing edge, the acceleration time history was asymmetrical and negative spikes can be observed. Similar patterns were reported in the published centrifuge studies [13] and were attributed to the large lateral deformations below the foundation corners (Fig. 11). The acceleration histories were, however, fairly symmetrical in other locations thanks to development of smaller shear strains.

The pore pressure-induced deamplification of input motion is due to separation of soil particles from each other that prevents the full transmission of propagating waves to the upper layers.

The contours of initial coordination number (average number of contacts per particle) and the minimum coordination number reached during the entire course of each simulation are provided in Fig. 16. It can be seen that before the application of base excitation, the coordination number in the models was generally higher than the threshold value of 4 required for a stable packing of particles [13]. In the free-field model, the coordination number dropped far below 4.0 during shaking everywhere within the deposit. It seems reasonable since, as shown in Fig. 8, the entire deposit liquefied in this case. This also explains the considerable drop in the acceleration amplitude in the free-field. In the soil-foundation system, the coordination number fell below 4 in most parts of the deposit but the reduction was not as significant as in the free-field and, therefore, the acceleration amplitudes were maintained at higher levels compared to the free-field. In the dilative region below the foundation, the minimum coordination number was evidently higher than the two sides due to lower EPPR in this area.

The cyclic shear stress-cyclic shear strain loops for the free-field model and the soil-light foundation system are presented in Fig. 17. The soil strength and stiffness deteriorated quickly after few loading cycles at all locations within the free-field deposit. The loops became almost perfectly horizontal by the end of simulation except for the bottom layer where the soil maintained some of its stiffness. For the soil-foundation system, the degradation of soil strength and stiffness was much less apparent, especially in the middle area below the footing (locations 9-12). According to this figure, the cyclic loops formed asymmetrical shapes at locations 5-8 and 13-16, which were located below the footing edges. These shapes were due to soil dilative behavior caused by the lateral spreading of particles in these regions and a temporary gain in soil strength and stiffness. The static shear stresses had different signs at locations 5-8 and 13-16. Therefore, the dilative behavior and orientation of the loops were in the opposite directions. Figure 18 shows the plots of cyclic shear stress versus shear strain (non-cyclic) for the soil-foundation system. The net horizontal shear strain was almost zero in the area under the footing centerline (locations 9-12) which is reasonable due to the model symmetry. However, development of large shear strains (around 30%) at locations below the footing edges can be seen (locations 5-8 and 13-16). According to the results, the accumulation of shear strain mainly occurred during periods of negative cyclic shear stress at locations 5-8. This is because of the fact that the total negative shear stress momentarily surpassed the soil shear strength due to the combined effect of the footing-induced negative static shear stresses and the negative cyclic shear stresses caused by the seismic loading. A similar argument can be made for locations 13-16 to explain why positive cyclic shear stresses result in large shear deformations.

The effective stress paths for the free-field deposit and the soil-foundation model are presented in Fig. 19. In the free-field, the confining effective stress and cyclic shear stress gradually reduced and almost disappeared everywhere in the deposit. This continuous reduction of confining effective stress during loading cycles, especially in the shallow layers, is indicative of soil contractive response in the free-field. Zero effective stress, however, was not reached at any location in the soil-foundation model and its reduction was noticeably less significant under the footing center (points 9-12). At locations 5 and 6, the inclination of the loops was to the left while it was in the opposite direction at points 13 and 14. The soil exhibited dilative behavior and temporarily regained some of its strength when the cyclic shear stress was negative at points 5 and 6. Therefore, considerably larger effective confining pressures were produced at negative cyclic shear stresses and the loops became inclined to the left. Conversely, at points 13 and 14, positive cyclic shear stresses led to dilative behavior and higher effective stresses.

4.2 Response of foundation block

Figure 20 shows the time histories of vertical forces (normalized by the footing weights) exerted on the foundation block by the fluid and the underlying soil as well as the total resultant force. The normalized fluid force reached the maximum value of approximately 0.25 during the simulation. As the excess pore pressure increased, a gradual reduction in the average force applied by the underlying soil occurred. It can be seen that the total normalized vertical force oscillated around the value of 1. According to this figure, the ground reaction was responsible for most of these fluctuations. After the end of loading, the pore pressure-induced force started to slowly decrease to the buoyancy force and the soil reaction force simultaneously increased.

Figure 21 demonstrates the plots of foundation settlement versus horizontal displacement, rotation and time. The net foundation sliding was to the left with an amount of approximately 5 mm. The cyclic horizontal displacements of the foundation were markedly larger during the first loading cycles and then they decreased as pore pressure continued to build up. According to the results, the net rotation of the foundation was approximately 0.005 rad. The final foundation settlement was higher than 40 cm, which indicates unacceptable levels of ground deformation by most design codes that cap the allowable settlement to 25 mm (e.g., [98]).

The plots of cyclic horizontal force-horizontal displacement and cyclic moment-rotation at the base center point of the foundation are presented in Fig. 22. The horizontal force and the moment acting on the foundation were obtained by directly monitoring the contact forces between the foundation block and the underlying soil, as well as the forces exerted by the fluid. The force-displacement loops cover relatively small areas, meaning that fairly small amount of energy was dissipated through the foundation sliding. The degradation of horizontal stiffness was negligible according to the results. However, a significant decrease in the amplitude of cyclic horizontal forces on the foundation during seismic loading can be seen. This can be explained by the decay of ground acceleration below the foundation due to partial loss of soil stiffness. The cyclic moment-rotation loops encompass much larger areas, signifying a higher level of rotational damping and energy dissipation during rocking motion. This plot exhibits highly non-linear behavior after the first few loading cycles. In addition, the rotational stiffness progressively reduced as the pore pressure buildup continued, and was recovered by the end of loading as the cyclic rotational movements diminished. According to this figure, the moment capacity gradually reduced as the shaking progressed. This, again, can be attributed to pore pressure-induced degradation of ground acceleration.

4.3 Effect of soil permeability

As mentioned earlier, the fluid viscosity in the models was initially set to 0.02 Pa.s (1.0 Pa.s in model units) which led to a soil permeability of approximately 3 mm/s. In this section, the same soil-foundation model is saturated with fluids with higher viscosities of 0.1 Pa.s and 0.2 Pa.s (5.0 Pa.s and 10.0 Pa.s in model units) to decrease the soil permeability to 0.6 mm/s and 0.3 mm/s, respectively, and the responses are discussed. The trends observed in this section are qualitatively compared to a similar centrifuge study conducted by Liu and Dobry [12].

Figure 23 shows the time histories of EPPR within the models with different values of the coefficient of permeability. According to this figure, away from the footing at locations 1-4, EPPR increased by decreasing the soil permeability. It can also be seen that the pore pressure dissipated at much lower rates in the deposits with the lower permeability. This trend was reversed near the footing and EPPR was generally smaller in the lower-permeability deposits, especially at locations

9-12. The temporary formation of negative EPPR was also observed at locations 5-6 and 9-10 in the deposits with coefficients of permeability of 0.6 mm/s and 0.3 mm/s. These observations are consistent with the results presented by Liu and Dobry [12].

This trend can be explained by the fact that the total excess pore pressure generated at each location is the sum of the local pore pressure buildup due to soil volumetric strain and the pore pressure induced by the migration of pore fluid within the deposit [12]. As the soil permeability decreases, the contribution of the second parameter reduces because the movement of pore fluid becomes more difficult and, as a result, the response gets closer to the undrained condition. The contours of the excess pore pressure at different time instants are provided in Fig. 24. As shown in Fig. 7, the net volumetric strain was positive below the footing due to the static shear stresses in this area while the side locations were less affected by the presence of footing and exhibited negative volumetric strain. Therefore, in the high-permeability deposit (Fig. 24a), larger excess pore pressures developed at the sides compared to the middle early in the simulation (t=2.5 s). This trend continued at t=5 s, however, despite the expansion of pore spaces below the footing, the excess pore pressure had positive values throughout the deposit. By the end of loading (t=8 s), the excess pore pressure equalized in the shallow layers and even higher pressures developed immediately below the foundation. Liu and Dobry [12] also reported larger maximum excess pore pressures below the footing compared to the sides in a highly pervious deposit, which was attributed to the fluid migration during loading and the higher capacity for pore pressure buildup due to larger confining pressures in this area. It can also be seen that the excess pore pressure almost completely dissipated in the model with the permeability of 3 mm/s by the end of simulation (t=20 s). In the deposits with lower permeability (Fig. 24b and c), relatively large negative excess pore pressures developed under the footing while the values were positive at the sides. These negative pressures existed until the end of loading (t=8 s) in the case of deposit with the lowest permeability (k=0.3 mm/s). In addition, it took much longer for the excess pore pressure to equalize at different depths in the lower-permeability deposits (k=0.6 mm/s and 0.3 mm/s). It is also worth noting that, except for the highest-permeability deposit (k=3 mm/s), the excess pore pressure did not fully dissipate by the end of simulations.

Figure 25 shows the vectors of fluid velocity relative to soil skeleton at different time instants on a plane perpendicular to the shaking direction and passing through the center of the footing inside the deposits with the permeability of 3 mm/s and 0.6 mm/s. The results for the deposit with the permeability of 0.3 mm/s are not shown due to very small fluid velocities that made the results difficult to interpret. It is evident from Fig. 25a that a strong fluid flow formed after a few seconds of shaking (t=2.5 s) from the sides toward the center in the model with the permeability of 3 mm/s, and its intensity increased as the dynamic loading progressed (t=5 s). This pore fluid migration quickly shrank the gap between the excess pore pressure at the sides and below the footing and, as shown in Fig. 24a, the excess pore pressure equalized even before the end of loading. During the dissipation phase (t=10 s), since the excess pore pressure reached higher values below the footing compared to the sides, the migration of pore fluid was mostly outward and away from the footing. According to Fig. 25b, the fluid velocity vectors during shaking were also mostly toward the center but with much lower magnitudes in the deposit with the lower permeability of 0.6 mm/s. This weak fluid flow postponed the equalization of excess pore pressure and, as demonstrated in Fig. 24b, the pressure gap remained large by the end of loading (t=8 s). Since the excess pore pressure was not evened out during shaking, the migration of pore fluid to the expansive zone below the footing continued even post-shaking (t=10 s).

Figure 26 shows the time histories of ground settlement below the footing and away from it near the left boundary of the soil-light foundation models with different soil permeability. According to this figure, decreasing the soil permeability resulted in lower footing settlement and ground upheaval. The total footing settlement was around 41.5 cm, 27.1 cm and 22.1 cm for the deposits with permeability of 3 mm/s, 0.6 m/s and 0.3 mm/s, respectively. The smaller ground deformation in the deposits with lower permeability was due the fact that smaller excess pore pressures developed below the footing in these cases and the soil maintained a larger magnitude of its strength and stiffness. While the total ground settlement decreased in the lower-permeability deposits, they experienced larger post-seismic settlements. The contribution of post-seismic settlement in the deposits with permeability of 3 mm/s, 0.6 mm/s and 0.3 mm/s was, respectively, 1.6%, 5.5% and 7.9% by the end of simulations. The final values could be higher (especially in the case of lower permeability) as the pore pressure did not completely dissipate by the end of simulations. These results are in agreement with the observations reported by [12]. In Fig. 27, the foundation settlement versus foundation width (both normalized by the thickness of the liquefiable soil layer) are shown along with the empirical boundary curves presented by Liu and Dobry [12] and the results of different centrifuge studies. It can be seen that the normalized foundation settlements recorded in this study fell within the predicted range. The time histories of footing acceleration are presented in Fig. 28. According to this figure, the footing experienced larger accelerations when the permeability of the underlying deposit was lower. This can be attributed to the milder degradation of soil stiffness in the lower-permeability deposits.

5 Conclusions

A fully coupled particle-based scheme was utilized in this paper to model the seismic response of shallow foundations resting on liquefiable soil. The soil was modeled as an assembly of rigid spherical particles using DEM and the fluid domain was discretized into a set of lumped fluid particles in SPH. The motion of the multiphase mixture was described by averaged forms of Navier-Stokes equations, and the interaction forces between the two phases were quantified utilizing well-established semi-empirical relations. The foundation was created using a collection of DEM particles glued together by high-stiffness parallel bonds to move as a single rigid block. The density of particles constituting the foundation block were adjusted to achieve the desired contact pressure. In addition, hybrid particles were placed at the block surface that interact with DEM particles and simulate impermeable boundaries for the SPH particles. In this study, each simulation took approximately 8 days (on average) to finish using a 52-core CPU.

A saturated soil-foundation system with an average contact pressure of 50 kPa was created using the described technique. Then it was subjected to a strong seismic base excitation and the response was analyzed and compared to the free-field. The results showed good consistency with the observations reported in the centrifuge studies. While the free-field model fully liquefied, EPPR was substantially lower in the soil-foundation system, especially in the zone below the footing. The lower liquefaction potential in this region was due to higher initial confining pressures and the static shear stresses produced by the footing that led to soil dilative behavior. The ground settlement was significantly larger under the footing compared to the free-field and exceeded acceptable design limits. This indicates that while the foundation soil did not reach full liquefaction marked by an EPPR of 1.0, there was enough stiffness degradation that led to large deformations. The large deformation occurred mainly near the foundation edges due to the relative ease of the soil to move laterally away from the footing and up to the ground surface as a result of the low confining pressure in those areas. The results showed that the ground deformation in the soil-foundation system was mainly due to deviatoric deformation and lateral outflow of particles below the footing that accumulated almost entirely during shaking. However, the deformation vectors in the free-field model were mostly vertical, indicating volumetric deformation. In addition, unlike the soil-foundation system, a large part of the free-field settlement occurred post-shaking. The results also suggest appreciably less degradation of soil strength and stiffness below the foundation due to lower EPPR developed in the expansive area. Much higher energy was dissipated during cyclic rotational movements of the foundation block than its horizontal movements. The degradation of rotational stiffness was also more significant compared to the horizontal stiffness.

Additional simulations were performed to analyze the effect of soil permeability on the seismic response of the soil-foundation model. The results revealed that as the soil permeability decreased, EPPR reduced below the footing while it increased at the sides of the model. This observation can be explained by the fact that the response in the lower-permeability deposits was closer to the undrained condition due to slower fluid flow. Furthermore, the total foundation settlement decreased by reducing soil permeability while the post-seismic settlement increased. The foundation acceleration was higher for the models with lower permeability because the soil maintained a larger magnitude of its stiffness. Results of performed simulations show that the proposed SPH-DEM framework can seamlessly model systems that involve soil-fluid-structure interaction.

Acknowledgement

This research was partially supported by the US Army Corps of Engineers Engineer Research and Development Center, grant number W9132V-13-C-0004 and the National Science Foundation award number CMMI-1728612. These supports are gratefully acknowledged.

References

[1] HB Seed and IM Idriss. Analysis of soil liquefaction: Niigata earthquake. *Journal of the Soil Mechanics and Foundations Division*, 93(3):83–108, 1967.

[2] Y Yoshimi and K Tokimatsu. Settlement of buildings on saturated sand during earthquakes. *Soils and Foundations*, 17(1):23–38, 1977.

[3] M Yasui. Settlement and inclination of reinforced concrete buildings in Dagupan City due to liquefaction during the 1990 Philippine earthquake. 1992.

[4] K Ishihara, AA Acacio, and I Towhata. Liquefaction-induced ground damage in Dagupan in the July 16, 1990 Luzon earthquake. *Soils and Foundations*, 33(1):133–154, 1993.

[5] N Yoshida, K Tokimatsu, S Yasuda, T Kokusho, and T Okimura. Geotechnical aspects of damage in Adapazari city during 1999 Kocaeli, Turkey earthquake. *Soils and foundations*, 41(4):25–45, 2001.

[6] R Verdugo and J González. Liquefaction-induced ground damages during the 2010 Chile earthquake. *Soil Dynamics and Earthquake Engineering*, 79:280–295, 2015.

[7] K Tokimatsu, S Tamura, H Suzuki, and K Katsumata. Building damage associated with geotechnical problems in the 2011 Tohoku Pacific Earthquake. *Soils and Foundations*, 52 (5):956–974, 2012.

[8] C Clifton, M Bruneau, G MacRae, R Leon, and A Fussell. Steel structures damage from the Christchurch earthquake series of 2010 and 2011. *Bulletin of the New Zealand Society for Earthquake Engineering*, 44(4):297–318, 2011.

[9] K Tokimatsu and HB Seed. Evaluation of settlements in sands due to earthquake shaking. *Journal of geotechnical engineering*, 113(8):861–878, 1987.

[10] K Ishihara and M Yoshimine. Evaluation of settlements in sand deposits following liquefaction during earthquakes. *Soils and foundations*, 32(1):173–188, 1992.

[11] S Dashti, JD Bray, JM Pestana, M Riemer, and D Wilson. Mechanisms of seismically induced settlement of buildings with shallow foundations on liquefiable soil. *Journal of geotechnical and geoenvironmental engineering*, 136(1):151–164, 2010.

[12] L Liu and R Dobry. Seismic response of shallow foundation on liquefiable sand. *Journal of geotechnical and geoenvironmental engineering*, 123(6):557–567, 1997.

[13] K Adalier, A Elgamal, J Meneses, and JI Baez. Stone columns as liquefaction countermeasure in non-plastic silty soils. *Soil Dynamics and Earthquake Engineering*, 23(7):571–584, 2003.

[14] S Dashti, JD Bray, JM Pestana, M Riemer, and D Wilson. Centrifuge testing to evaluate and mitigate liquefaction-induced building settlement mechanisms. *Journal of geotechnical and geoenvironmental engineering*, 136(7):918–929, 2010.

[15] CP Hayden, JD Zupan, JD Bray, JD Allmond, and BL Kutter. Centrifuge tests of adjacent mat-supported buildings affected by liquefaction. *Journal of Geotechnical and Geoenvironmental Engineering*, 141(3):04014118, 2015.

[16] R Rasouli, I Towhata, and T Akima. Experimental evaluation of drainage pipes as a mitigation against liquefaction-induced settlement of structures. *Journal of Geotechnical and Geoenvironmental Engineering*, 142(9):04016041, 2016.

[17] A Zeybek and SPG Madabhushi. Influence of air injection on the liquefaction-induced deformation mechanisms beneath shallow foundations. *Soil Dynamics and Earthquake Engineering*, 97:266–276, 2017.

[18] B Mehrzad, Y Jafarian, CJ Lee, and AH Haddad. Centrifuge study into the effect of liquefaction extent on permanent settlement and seismic response of shallow foundations. *Soils and foundations*, 58(1):228–240, 2018.

[19] O Adamidis and SPG Madabhushi. Deformation mechanisms under shallow foundations on liquefiable layers of varying thickness. *Géotechnique*, 68(7):602–613, 2018.

[20] R Kumar, M Sawaishi, K Horikoshi, and A Takahashi. Centrifuge modeling of hybrid foundation to mitigate liquefaction-induced effects on shallow foundation resting on liquefiable ground. *Soils and Foundations*, 59(6):2083–2098, 2019.

[21] KM Darby, GL Hernandez, JT DeJong, RW Boulanger, MG Gomez, and DW Wilson. Centrifuge model testing of liquefaction mitigation via microbially induced calcite precipitation. *Journal of Geotechnical and Geoenvironmental Engineering*, 145(10):04019084, 2019.

[22] A Zeybek, SPG Madabhushi, and L Pelecanos. Seismic response of partially saturated soils beneath shallow foundations under sequential ground motions. *Bulletin of Earthquake Engineering*, 18(5):1987–2002, 2020.

[23] A Zeybek and SPG Madabhushi. Centrifuge testing to evaluate the liquefaction response of air-injected partially saturated soils beneath shallow foundations. *Bulletin of Earthquake Engineering*, 15(1):339–356, 2017.

[24] R Popescu and JH Prevost. Centrifuge validation of a numerical model for dynamic soil liquefaction. *Soil Dynamics and Earthquake Engineering*, 12(2):73–90, 1993.

[25] A Elgamal, J Lu, and Z Yang. Liquefaction-induced settlement of shallow foundations and remediation: 3D numerical simulation. *Journal of earthquake engineering*, 9(spec01):17–45, 2005.

[26] R Popescu, JH Prevost, G Deodatis, and P Chakrabortty. Dynamics of nonlinear porous media with applications to soil liquefaction. *Soil dynamics and earthquake engineering*, 26 (6-7):648–665, 2006.

[27] F Lopez-Caballero and AM Farahmand-Razavi. Numerical simulation of liquefaction effects on seismic SSI. *Soil Dynamics and Earthquake Engineering*, 28(2):85–98, 2008.

[28] H Shahir and A Pak. Estimating liquefaction-induced settlement of shallow foundations by numerical approach. *Computers and Geotechnics*, 37(3):267–279, 2010.

[29] KI Andrianopoulos, AG Papadimitriou, and GD Bouckovalas. Bounding surface plasticity model for the seismic liquefaction analysis of geostructures. *Soil Dynamics and Earthquake Engineering*, 30(10):895–911, 2010.

[30] DK Karamitros, GD Bouckovalas, and YK Chaloulos. Insight into the seismic liquefaction performance of shallow foundations. *Journal of Geotechnical and Geoenvironmental Engineering*, 139(4):599–607, 2013.

[31] Z Karimi and S Dashti. Numerical and centrifuge modeling of seismic soil–foundation–structure interaction on liquefiable ground. *Journal of Geotechnical and Geoenvironmental Engineering*, 142(1):04015061, 2016.

[32] P Ayoubi and A Pak. Liquefaction-induced settlement of shallow foundations on two-layered subsoil strata. *Soil Dynamics and Earthquake Engineering*, 94:35–46, 2017.

[33] VE Dimitriadi, GD Bouckovalas, YK Chaloulos, and AS Aggelis. Seismic liquefaction performance of strip foundations: effect of ground improvement dimensions. *Soil Dynamics and Earthquake Engineering*, 106:298–307, 2018.

[34] Jorge Macedo and Jonathan D Bray. Key trends in liquefaction-induced building settlement. *Journal of Geotechnical and Geoenvironmental Engineering*, 144(11):04018076, 2018.

[35] A Hasheminezhad and H Bahadori. Seismic response of shallow foundations over liquefiable soils improved by deep soil mixing columns. *Computers and Geotechnics*, 110:251–273, 2019.

[36] CW Lu, MC Chu, L Ge, and KS Peng. Estimation of settlement after soil liquefaction for structures built on shallow foundations. *Soil Dynamics and Earthquake Engineering*, 129: 105916, 2020.

[37] S Cong, L Tang, X Ling, L Geng, and J Lu. Numerical analysis of liquefaction-induced differential settlement of shallow foundations on an island slope. *Soil Dynamics and Earthquake Engineering*, 140:106453, 2021.

[38] K Kassas, O Adamidis, N Gerolymos, and I Anastasopoulos. Numerical modelling of a structure with shallow strip foundation during earthquake-induced liquefaction. *Géotechnique*, pages 1–15, 2020.

[39] AG Özcebe, D Giretti, F Bozzoni, V Fioravante, and CG Lai. Centrifuge and numerical mod-

elling of earthquake-induced soil liquefaction under free-field conditions and by considering soil–structure interaction. *Bulletin of Earthquake Engineering*, 19(1):47–75, 2021.

[40] U El Shamy. Multiscale modelling of the seismic response of shallow foundations on saturated granular soils. *Geomechanics and Geoengineering*, pages 1–22, 2021.

[41] U El Shamy and M Zeghal. Coupled continuum-discrete model for saturated granular soils. *Journal of Engineering Mechanics*, 131(4):413–426, 2005.

[42] U El Shamy, M Zeghal, R Dobry, S Thevanayagam, A Elgamal, T Abdoun, C Medina, R Bethapudi, and V Bennett. Micromechanical aspects of liquefaction-induced lateral spreading. *International Journal of Geomechanics*, 10(5):190–201, 2010.

[43] N Ravichandran, B Machmer, H Krishnapillai, and K Meguro. Micro-scale modeling of saturated sandy soil behavior subjected to cyclic loading. *Soil Dynamics and Earthquake Engineering*, 30(11):1212–1225, 2010.

[44] N Abdoulaye Hama, T Ouahbi, S Taibi, H Souli, JM Fleureau, and A Pantet. Analysis of mechanical behaviour and internal stability of granular materials using discrete element method. *International Journal for Numerical and Analytical Methods in Geomechanics*, 40 (12):1712–1729, 2016.

[45] L Jing, CY Kwok, YF Leung, and YD Sobral. Extended CFD-DEM for free-surface flow with multi-size granules. *International Journal for Numerical and Analytical Methods in Geomechanics*, 40(1):62–79, 2016.

[46] X Li and J Zhao. A unified CFD-DEM approach for modeling of debris flow impacts on flex-

ible barriers. *International Journal for Numerical and Analytical Methods in Geomechanics*, 42(14):1643–1670, 2018.

[47] Y Liu, L Wang, Y Hong, J Zhao, and ZY Yin. A coupled CFD-DEM investigation of suffusion of gap graded soil: Coupling effect of confining pressure and fines content. *International Journal for Numerical and Analytical Methods in Geomechanics*, 44(18):2473–2500, 2020.

[48] M Kanitz and J Grabe. The influence of the void fraction on the particle migration: A coupled computational fluid dynamics–discrete element method study about drag force correlations. *International Journal for Numerical and Analytical Methods in Geomechanics*, 45(1):45–63, 2021.

[49] YI Zhu, PJ Fox, and JP Morris. A pore-scale numerical model for flow through porous media. *International Journal for Numerical and Analytical Methods in Geomechanics*, 23 (9):881–904, 1999.

[50] AV Potapov, ML Hunt, and CS Campbell. Liquid–solid flows using smoothed particle hydrodynamics and the discrete element method. *Powder Technology*, 116(2-3):204–213, 2001.

[51] Y Han and PA Cundall. Lattice boltzmann modeling of pore-scale fluid flow through idealized porous media. *International Journal for Numerical Methods in Fluids*, 67(11):1720–1734, 2011.

[52] DF Boutt, BK Cook, and JR Williams. A coupled fluid–solid model for problems in geomechanics: application to sand production. *International Journal for Numerical and Analytical Methods in Geomechanics*, 35(9):997–1018, 2011.

[53] Y Fukumoto, H Yang, T Hosoyamada, and S Ohtsuka. 2-D coupled fluid-particle numerical analysis of seepage failure of saturated granular soils around an embedded sheet pile with no macroscopic assumptions. *Computers and Geotechnics*, 136:104234, 2021.

[54] E Catalano, B Chareyre, and E Barthélemy. Pore-scale modeling of fluid-particles interaction and emerging poromechanical effects. *International Journal for Numerical and Analytical Methods in Geomechanics*, 38(1):51–71, 2014.

[55] U El Shamy and Y Abdelhamid. Modeling granular soils liquefaction using coupled lattice boltzmann method and discrete element method. *Soil Dynamics and Earthquake Engineering*, 67:119–132, 2014.

[56] Y Abdelhamid and U El Shamy. Pore-scale modeling of fine-particle migration in granular filters. *International Journal of Geomechanics*, 16(3):04015086, 2016.

[57] K Han, YT Feng, and DRJ Owen. Numerical simulations of irregular particle transport in turbulent flows using coupled LBM-DEM. *Computer Modeling in Engineering and Sciences*, 18(2):87, 2007.

[58] W Zhong, A Yu, X Liu, Z Tong, and H Zhang. DEM/CFD-DEM modelling of non-spherical particulate systems: theoretical developments and applications. *Powder technology*, 302: 108–152, 2016.

[59] M Wang, YT Feng, and CY Wang. Coupled bonded particle and lattice Boltzmann method for modelling fluid-solid interaction. *International Journal for Numerical and Analytical Methods in Geomechanics*, 40(10):1383–1401, 2016.

[60] M Gardner and N Sitar. Coupled three-dimensional discrete element-lattice Boltzmann methods for fluid-solid interaction with polyhedral particles. *International Journal for Numerical and Analytical Methods in Geomechanics*, 43(14):2270–2287, 2019.

[61] M Wang, Y Feng, and T Qu. On the implicit immersed boundary method in coupled discrete element and lattice Boltzmann method. *International Journal for Numerical and Analytical Methods in Geomechanics*, 44(4):516–532, 2020.

[62] H Cheng, S Luding, N Rivas, J Harting, and V Magnanimo. Hydro-micromechanical modeling of wave propagation in saturated granular crystals. *International journal for numerical and analytical methods in geomechanics*, 43(5):1115–1139, 2019.

[63] Z Benseghier, P Cuéllar, LH Luu, S Bonelli, and P Philippe. A parallel GPU-based computational framework for the micromechanical analysis of geotechnical and erosion problems. *Computers and Geotechnics*, 120:103404, 2020.

[64] M Krzaczek, M Nitka, and J Tejchman. Effect of gas content in macropores on hydraulic fracturing in rocks using a fully coupled DEM/CFD approach. *International Journal for Numerical and Analytical Methods in Geomechanics*, 45(2):234–264, 2021.

[65] X Sun, M Sakai, and Y Yamada. Three-dimensional simulation of a solid–liquid flow by the dem–sph method. *Journal of Computational Physics*, 248:147–176, 2013.

[66] D Markauskas, H Kruggel-Emden, and V Scherer. Numerical analysis of wet plastic particle separation using a coupled dem-sph method. *Powder Technology*, 325:218–227, 2018.

[67] D Markauskas and H Kruggel-Emden. Coupled dem-sph simulations of wet continuous screening. *Advanced Powder Technology*, 30(12):2997–3009, 2019.

[68] JW Fernandez, PW Cleary, MD Sinnott, and RD Morrison. Using sph one-way coupled to dem to model wet industrial banana screens. *Minerals Engineering*, 24(8):741–753, 2011.

[69] MD Sinnott, PW Cleary, and RD Morrison. Combined dem and sph simulation of overflow ball mill discharge and trommel flow. *Minerals Engineering*, 108:93–108, 2017.

[70] PW Cleary. Prediction of coupled particle and fluid flows using dem and sph. *Minerals Engineering*, 73:85–99, 2015.

[71] HCP Karunasena, W Senadeera, YT Gu, and RJ Brown. A coupled sph-dem model for micro-scale structural deformations of plant cells during drying. *Applied Mathematical Modelling*, 38(15-16):3781–3801, 2014.

[72] K Wu, D Yang, and N Wright. A coupled sph-dem model for fluid-structure interaction problems with free-surface flow and structural failure. *Computers & Structures*, 177:141–161, 2016.

[73] U El Shamy and SF Sizkow. Coupled smoothed particle hydrodynamics-discrete element method simulations of soil liquefaction and its mitigation using gravel drains. *Soil Dynamics and Earthquake Engineering*, 140:106460, 2021.

[74] SF Sizkow and U El Shamy. SPH-DEM simulations of saturated granular soils liquefaction incorporating particles of irregular shape. *Computers and Geotechnics*, 134:104060, 2021.

[75] U El Shamy and SF Sizkow. Coupled SPH-DEM simulations of liquefaction-induced flow failure. *Soil Dynamics and Earthquake Engineering*, 144:106683, 2021.

[76] SF Sizkow and U El Shamy. A comparison between coupled SPH-DEM and LBM-DEM approaches for soil liquefaction. In *IFCEE*, pages 53–60. 2021.

[77] SF Sizkow and U El Shamy. Seismic response analysis of submerged slopes using coupled SPH-DEM scheme. *International Journal of Geomechanics*, 2021 (Under review).

[78] JJ Monaghan. Smoothed particle hydrodynamics. *Annual Review of Astronomy and Astrophysics*, 30(1):543–574, 1992.

[79] CGI Itasca. Pfc3d (particle flow code in 3 dimensions), version 6.0. *Minneapolis: ICG*, 2019.

[80] Yi He, AE Bayly, A Hassanpour, F Muller, K Wu, and D Yang. A gpu-based coupled sph-dem method for particle-fluid flow with free surfaces. *Powder Technology*, 338:548–562, 2018.

[81] K Wu, D Yang, N W, and A Khan. An integrated particle model for fluid-particle-structure interaction problems with free-surface flow and structural failure. *Journal of Fluids and Structures*, 76:166–184, 2018.

[82] M Robinson, M Ramaioli, and S Luding. Fluid–particle flow simulations using two-way-coupled mesoscale sph–dem and validation. *International Journal of Multiphase Flow*, 59: 121–134, 2014.

[83] W Dehnen and H Aly. Improving convergence in smoothed particle hydrodynamics simulations without pairing instability. *Monthly Notices of the Royal Astronomical Society*, 425 (2):1068–1082, 2012.

[84] JP Morris, PJ Fox, and Y Zhu. Modeling low reynolds number incompressible flows using sph. *Journal of Computational Physics*, 136(1):214–226, 1997.

[85] JJ Monaghan. Sph without a tensile instability. *Journal of Computational Physics*, 159(2): 290–311, 2000.

[86] JJ Monaghan. Simulating free surface flows with sph. *Journal of Computational Physics*, 110(2):399–406, 1994.

[87] S Adami, XY Hu, and NA Adams. A generalized wall boundary condition for smoothed particle hydrodynamics. *Journal of Computational Physics*, 231(21):7057–7075, 2012.

[88] K Iwashita and M Oda. Rolling resistance at contacts in simulation of shear band development by dem. *Journal of Engineering Mechanics*, 124(3):285–292, 1998.

[89] M Oda, J Konishi, and S Nemat-Nasser. Experimental micromechanical evaluation of strength of granular materials: effects of particle rolling. *Mechanics of Materials*, 1(4): 269–283, 1982.

[90] F Calvetti, G Combe, and J Lanier. Experimental micromechanical analysis of a 2d granular material: relation between structure evolution and loading path. *Mechanics of Cohesive-frictional Materials: An International Journal on Experiments, Modelling and Computation of Materials and Structures*, 2(2):121–163, 1997.

[91] A Misra and H Jiang. Measured kinematic fields in the biaxial shear of granular materials. *Computers and Geotechnics*, 20(3-4):267–285, 1997.

[92] U El Shamy and C Denissen. Microscale characterization of energy dissipation mechanisms in liquefiable granular soils. *Computers and Geotechnics*, 37(7-8):846–857, 2010.

[93] D Markauskas, H Kruggel-Emden, R Sivanesapillai, and H Steeb. Comparative study on mesh-based and mesh-less coupled CFD-DEM methods to model particle-laden flow. *Powder Technology*, 305:78–88, 2017.

[94] S Ergun. Fluid flow through packed columns. *Chem. Eng. Prog.*, 48:89–94, 1952.

[95] RR Trussell and M Chang. Review of flow through porous media as applied to head loss in water filters. *Journal of Environmental Engineering*, 125(11):998–1006, 1999.

[96] J Garnier, C Gaudin, SM Springman, PJ Culligan, D Goodings, D Konig, B Kutter, R Phillips, MF Randolph, and L Thorel. Catalogue of scaling laws and similitude questions in geotechnical centrifuge modelling. *International Journal of Physical Modelling in Geotechnics*, 7(3):01–23, 2007.

[97] PC Carman. Fluid flow through granular beds. *Trans. Inst. Chem. Eng.*, 15:150–166, 1937.

[98] B Das. Principles of Geotechnical Engineering (Seven Edition), 2010.

[99] P Coelho. Shallow foundations exposed to seismic liquefaction: a centrifuge based study on the level and mitigation of the effects. *SERIES report*, 2013.

[100] D Bertalot, AJ Brennan, and FA Villalobos. Influence of bearing pressure on liquefaction-induced settlement of shallow foundations. *Géotechnique*, 63(5):391–399, 2013.

[101] EA Hausler. *Influence of ground improvement on settlement and liquefaction: A study based*

on field case history evidence and dynamic geotechnical centrifuge tests. University of California, Berkeley, 2002.

Table 1: Simulations details in model units

Soil deposit	
Particle size	1.5 mm to 2.5 mm
Normal stiffness	5.0×10^{5} N/m
Shear stiffness	5.0×10^{5} N/m
Normal critical damping ratio	0.1
Shear critical damping ratio	0.0
Friction coefficient	0.5
Rolling friction coefficient	0.2
Density	2650 kg/m^3
Approx. number of particles	215000
Viscous Fluid	
Initial spacing	4 mm
Kernel radius	6 mm
Dynamic viscosity	1.0-10.0 Pa.s
Density	1000 kg/m^3
Computation parameters	
g-level	50
Time step for DEM	5×10^{-7} s
Time step for SPH	2×10^{-6} s

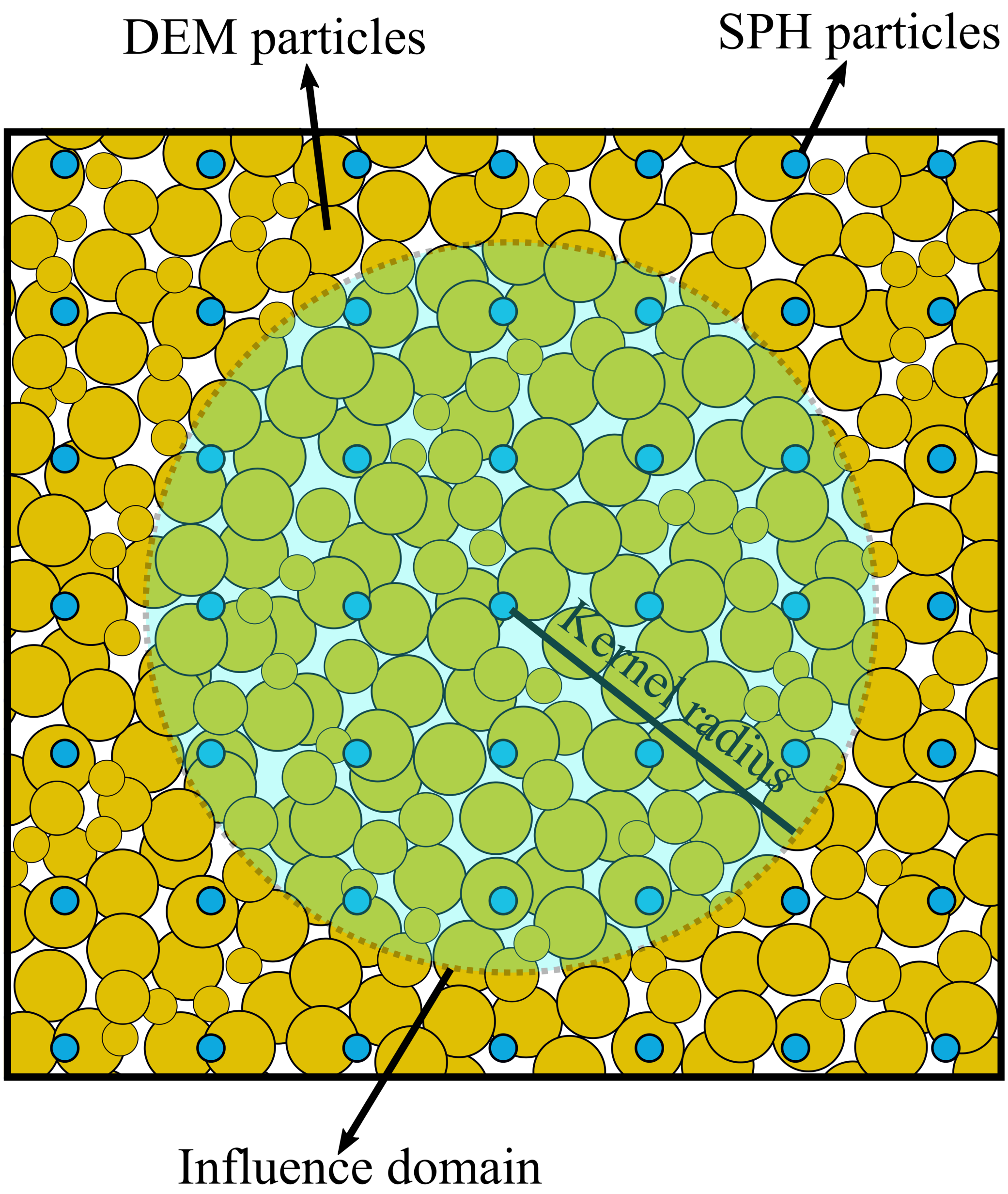

Figure 1: A schematic view of the SPH-DEM model

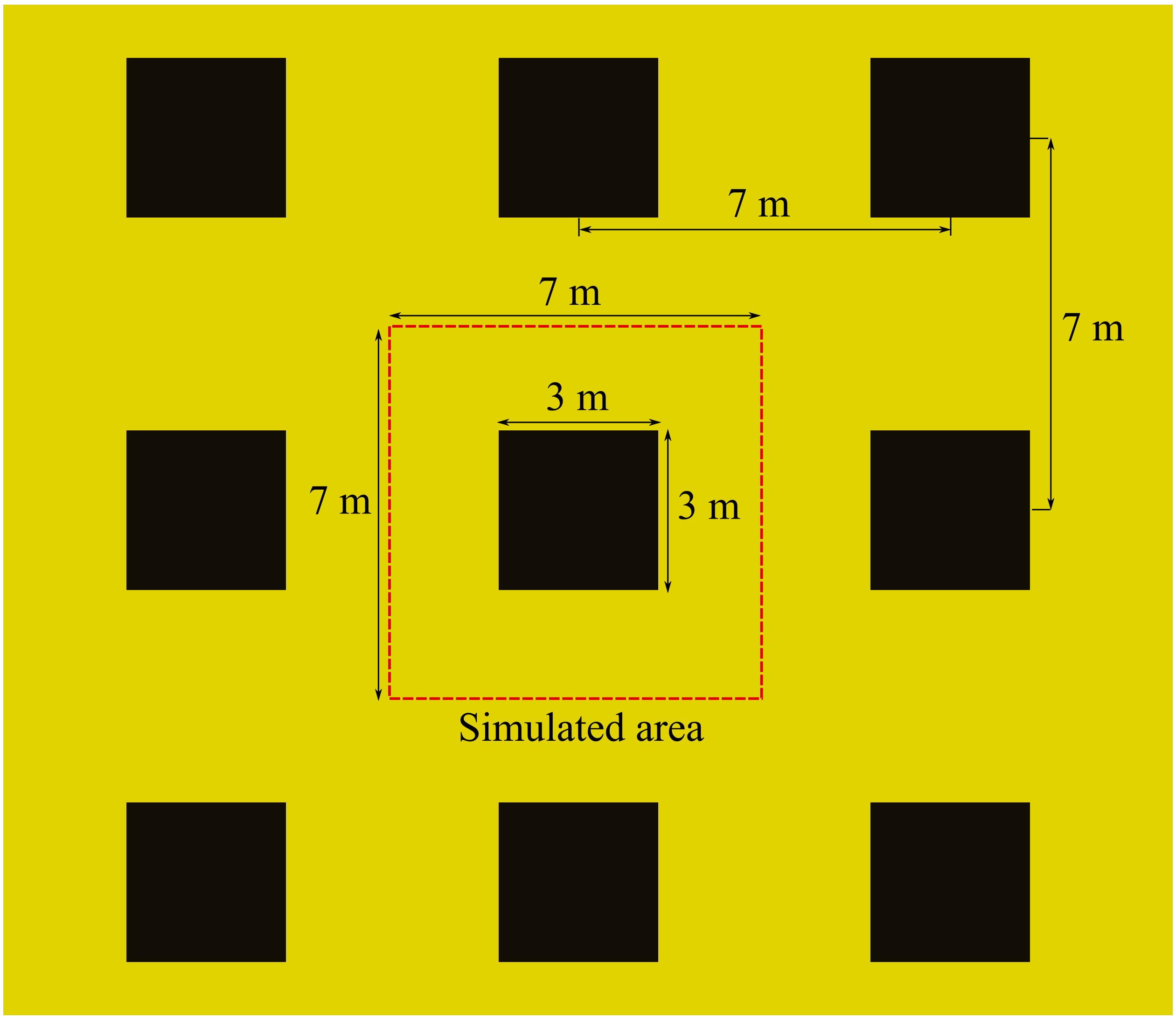

Figure 2: Schematic configuration of the shallow foundations along with the selected simulation zone

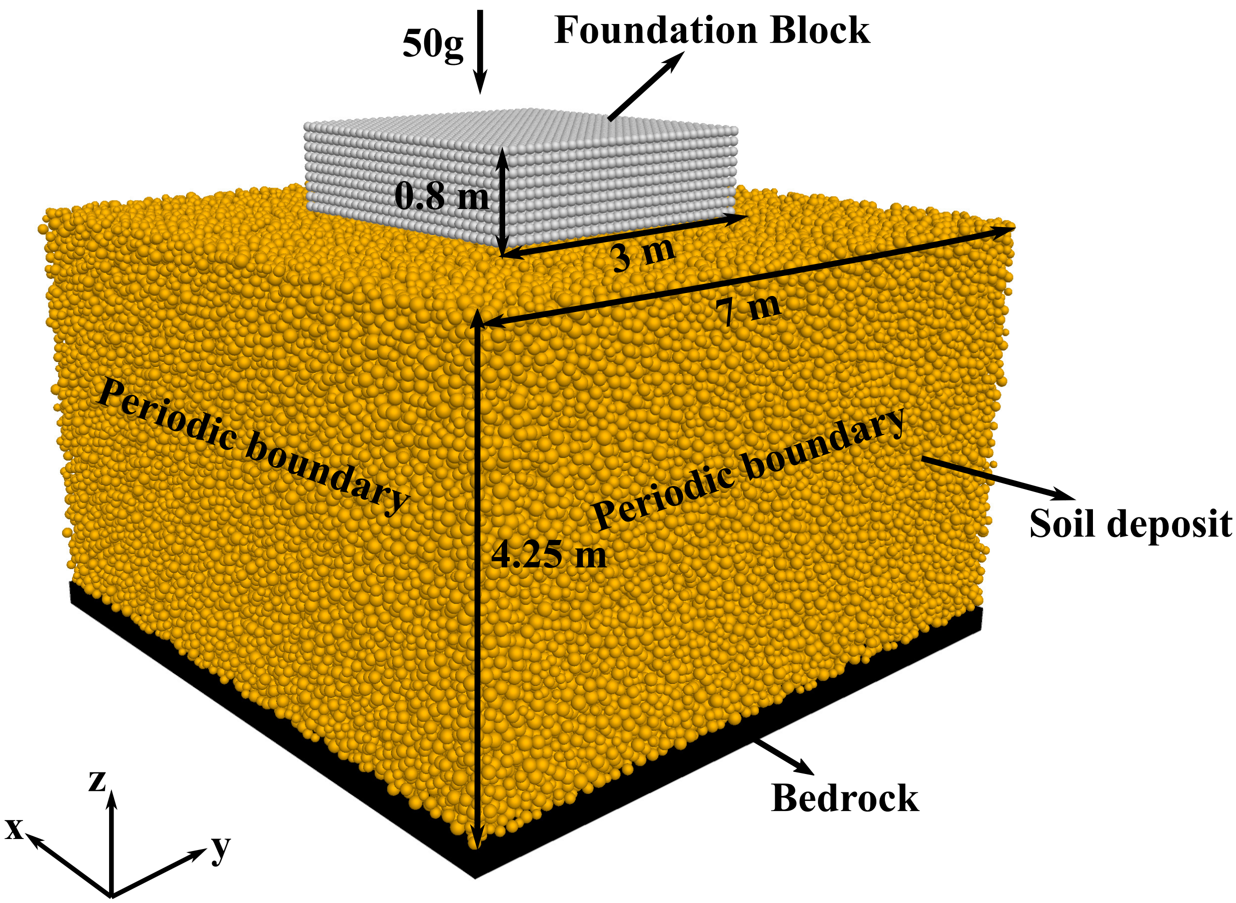

Figure 3: 3D view of the modeled soil-footing system

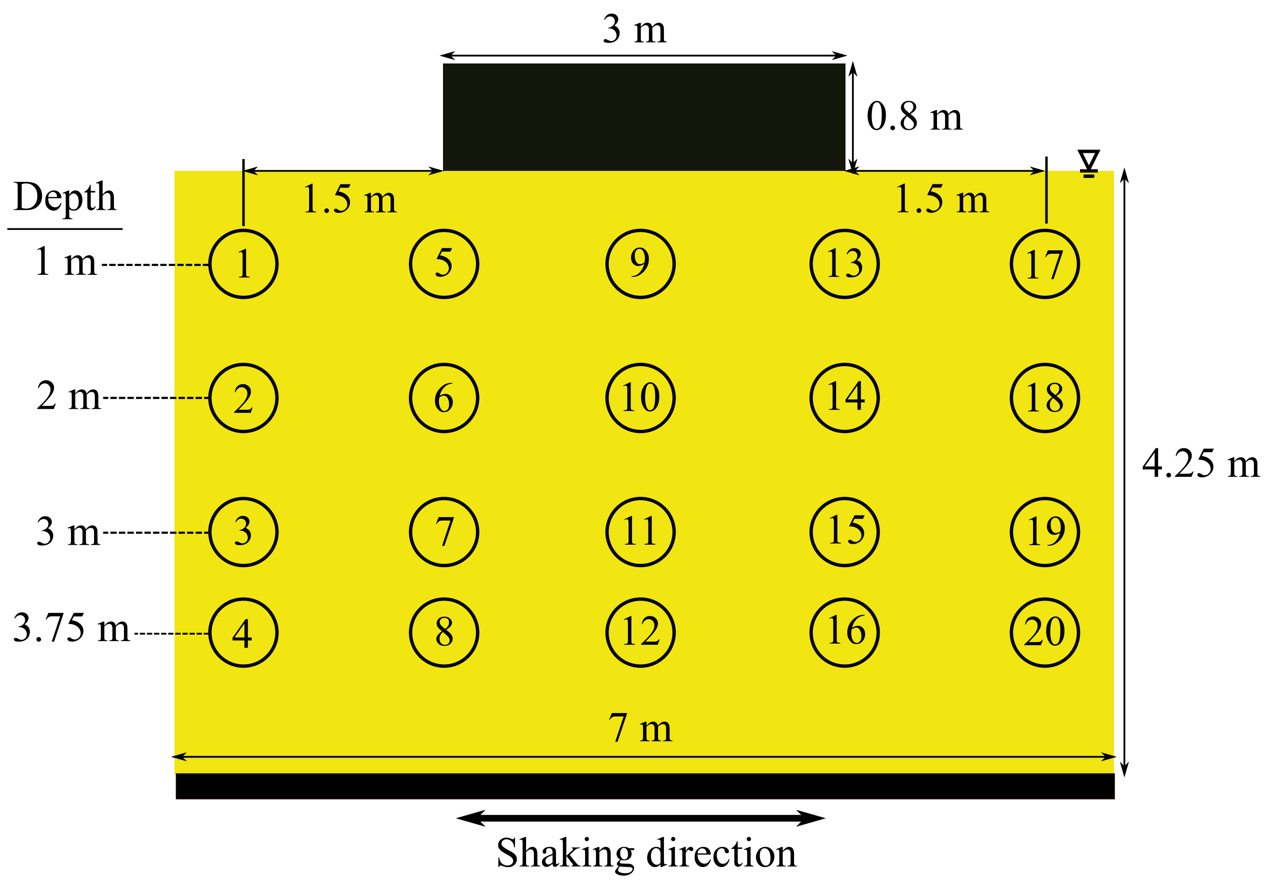

Figure 4: Location of measurement volumes within the deposits

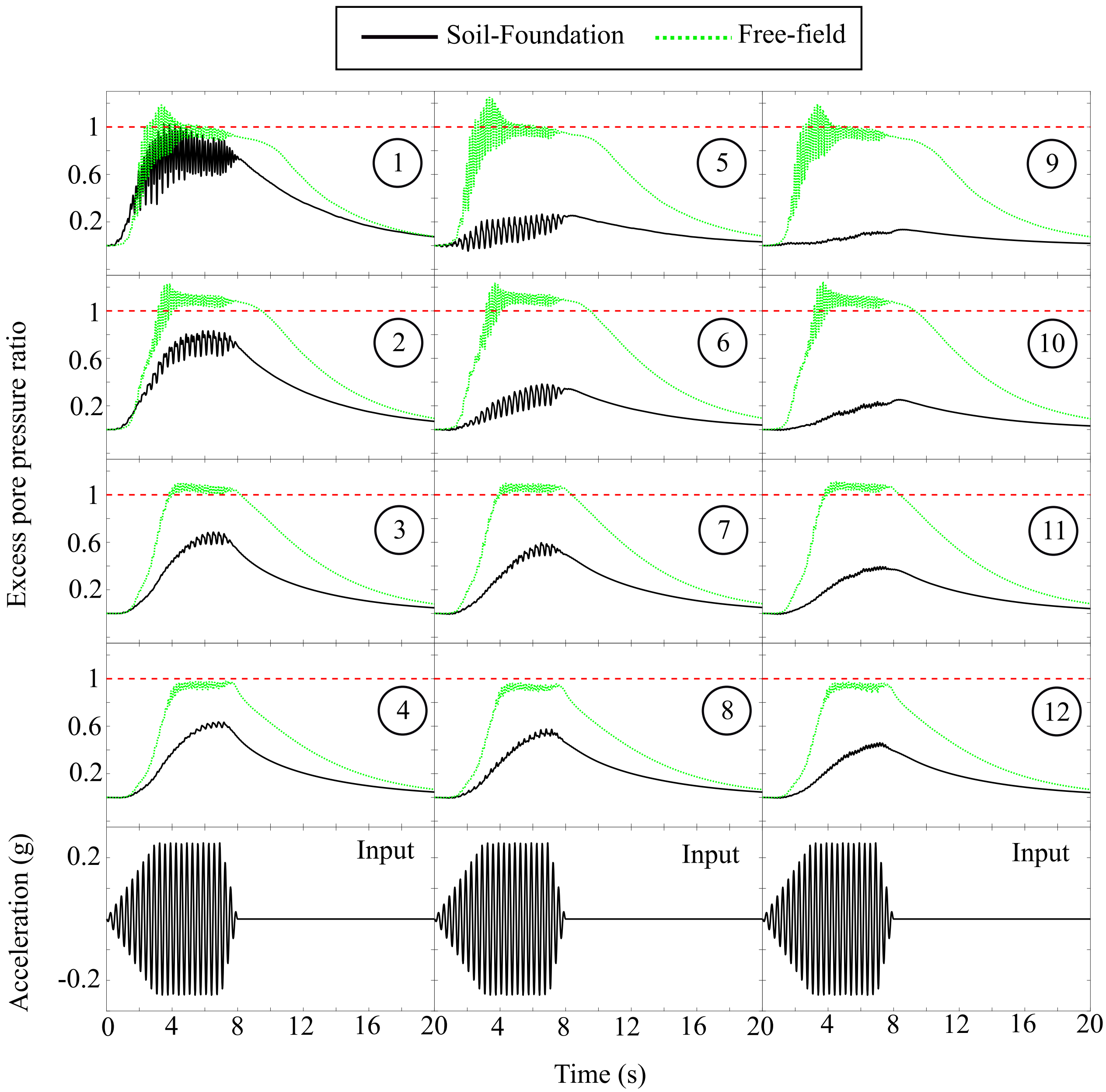

Figure 5: Time histories of excess pore pressure ratio at different measurement locations

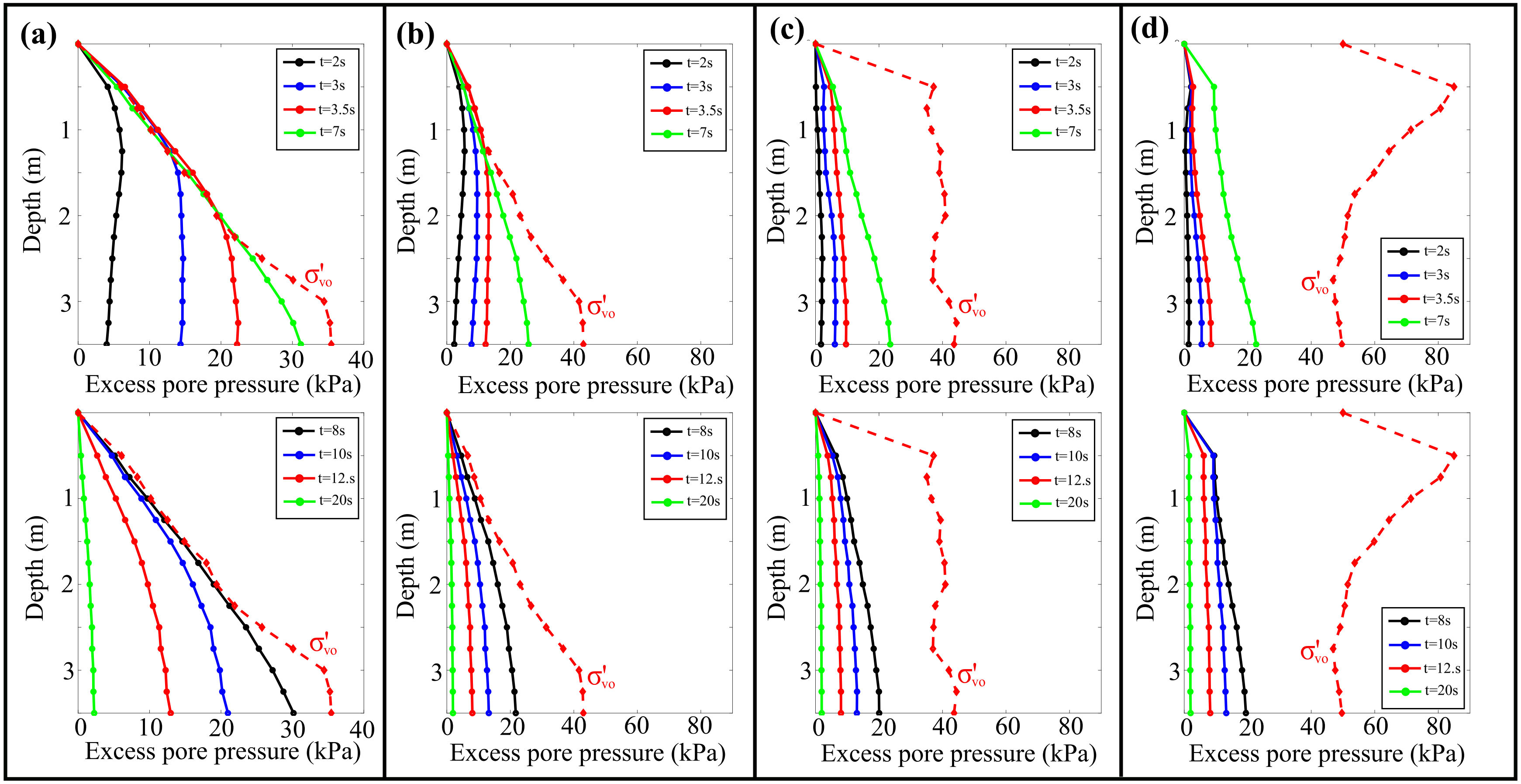

Figure 6: Profiles of excess pore pressure at selected time instants (a) in the free-field, (b) near the left boundary of the soil-foundation system, (c) below the foundation edge, and (d) below the foundation center

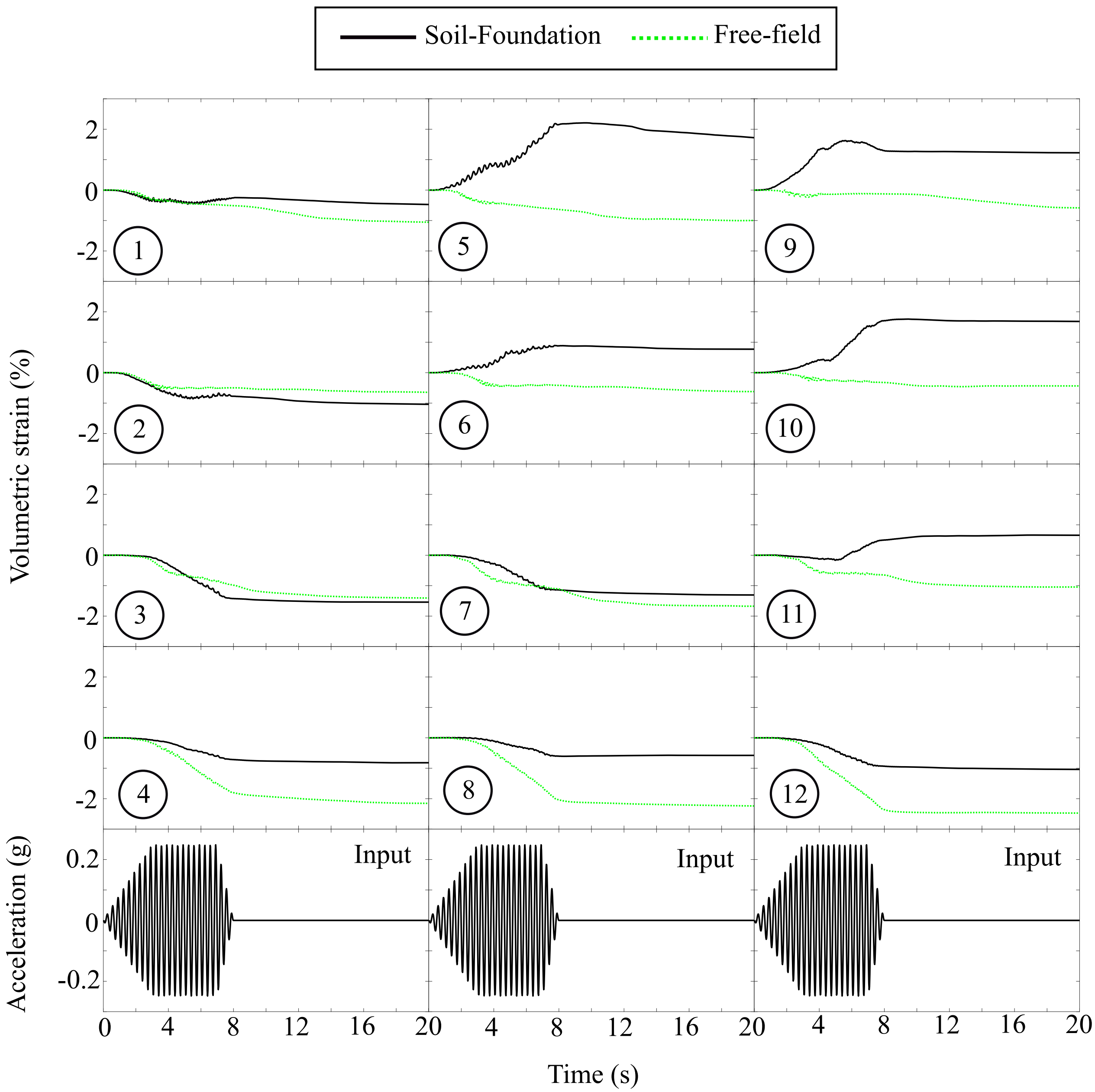

Figure 7: Time histories of volumetric strain at different measurement locations

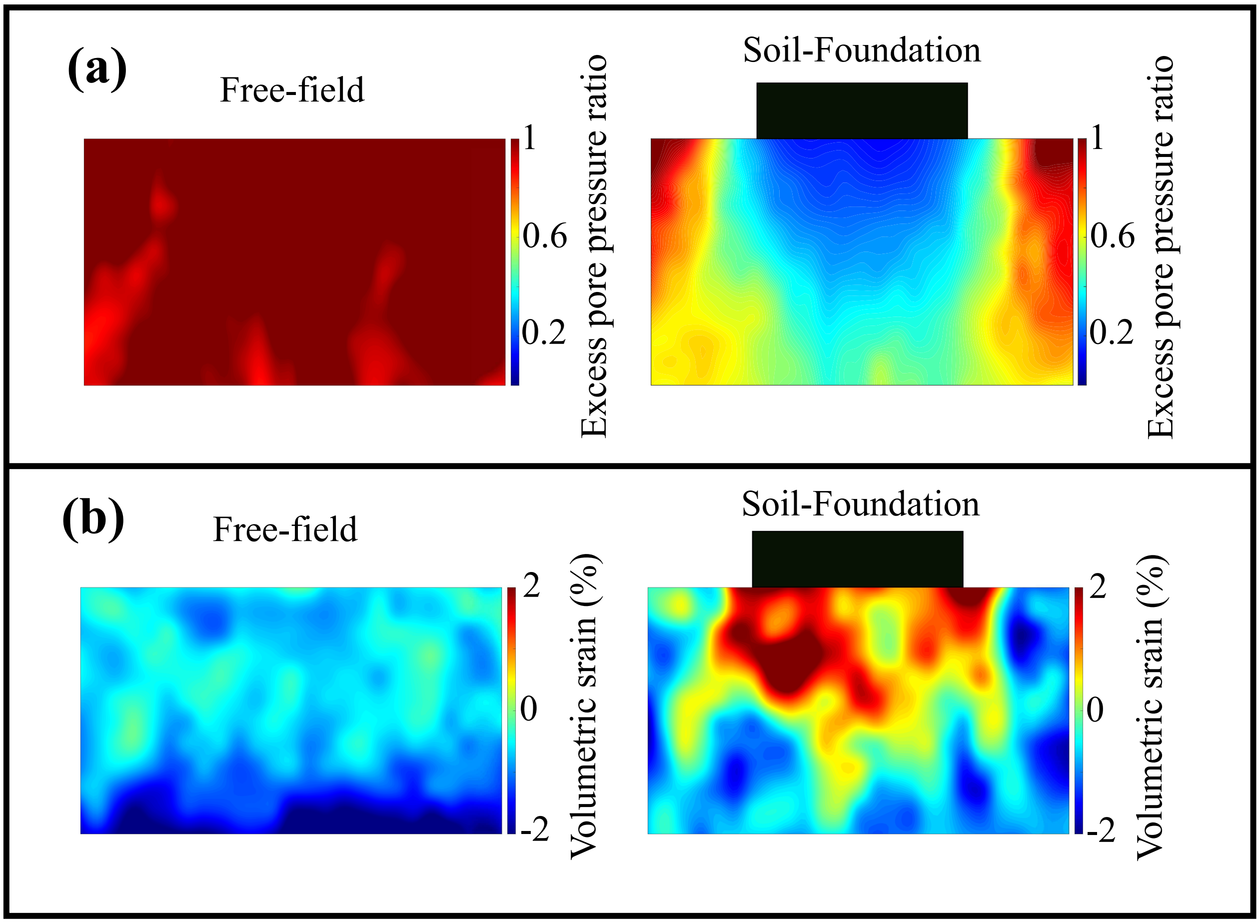

Figure 8: Contours of (a) maximum excess pore pressure ratio reached during the course of each simulation, and (b) total volumetric strain at the end of simulations

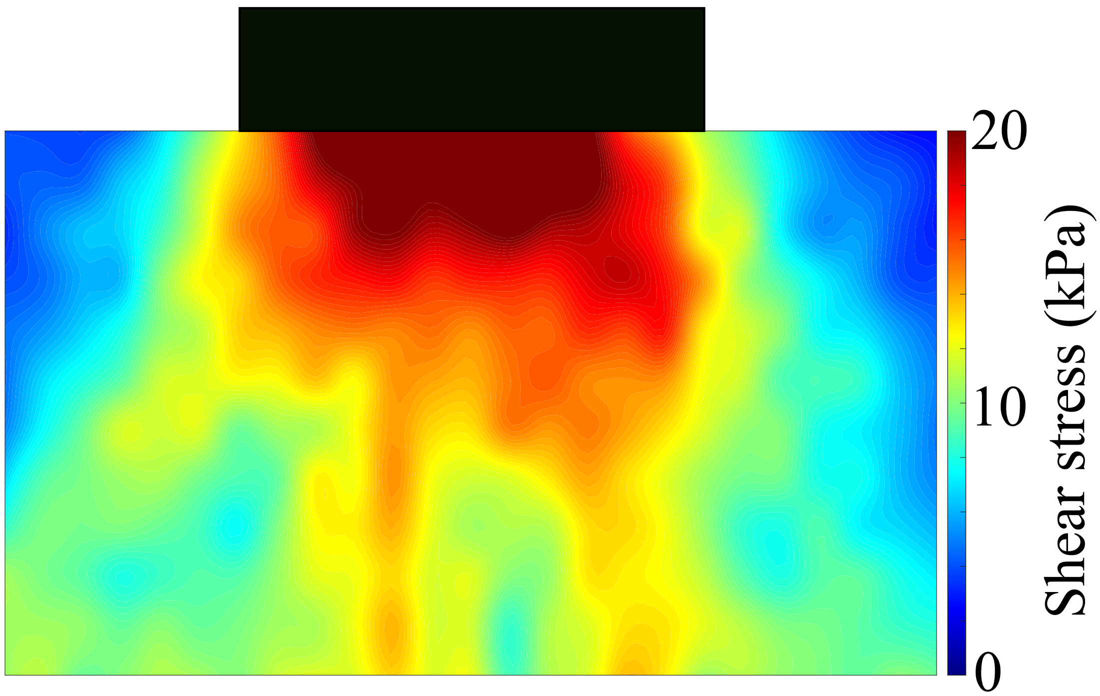

Figure 9: Contour of maximum initial shear stress inside the deposit overlain by the foundation

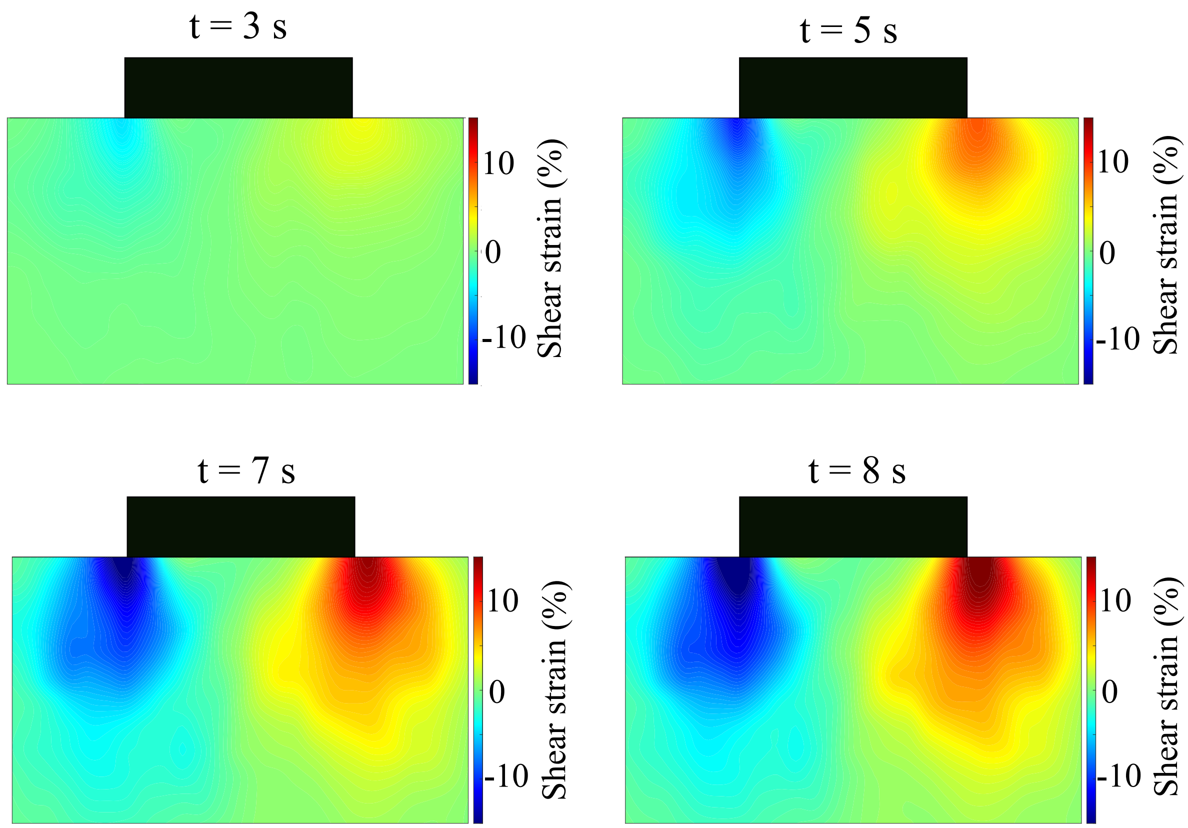

Figure 10: Contours of shear strain at different time instants inside the soil-foundation system

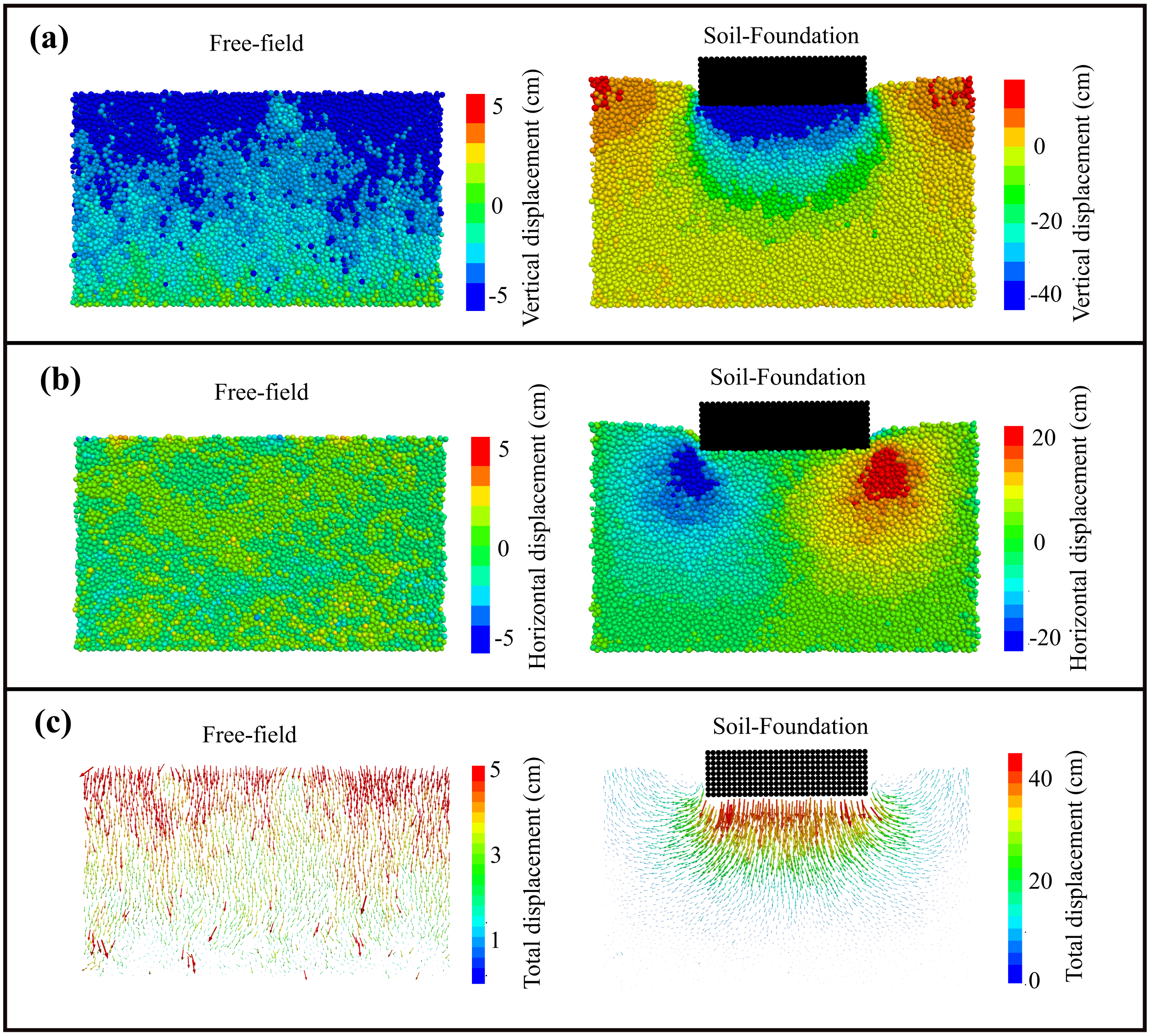

Figure 11: Contours of (a) vertical displacement, (b) horizontal displacement, and (c) total displacement

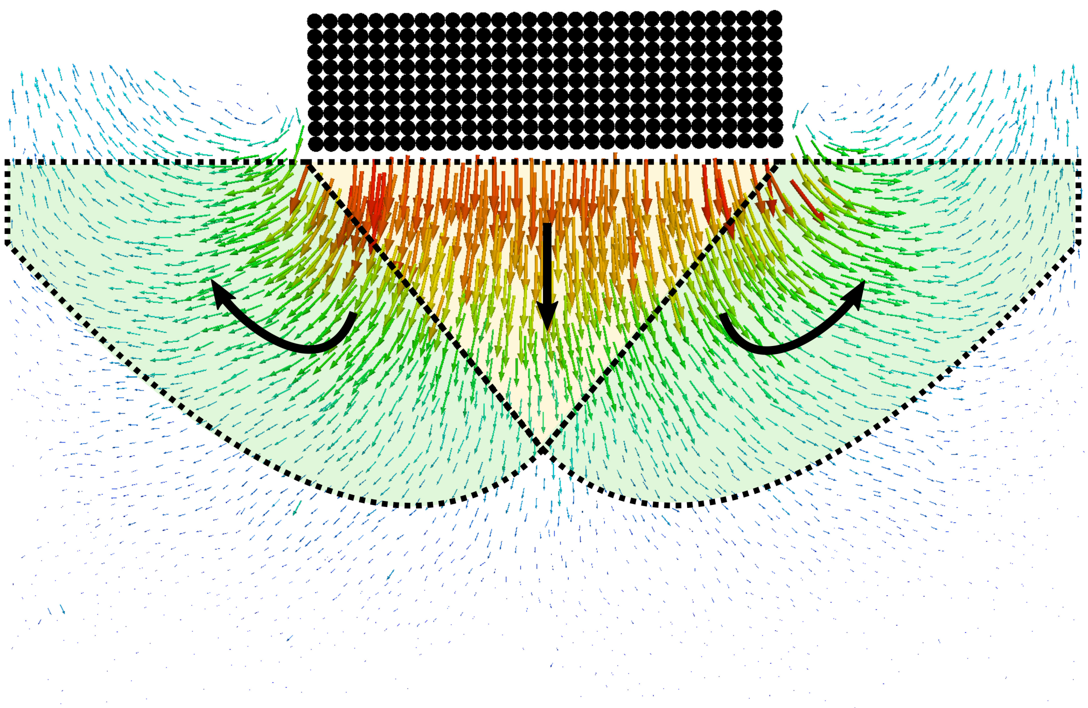

Figure 12: Deformation mechanism in the soil-foundation system

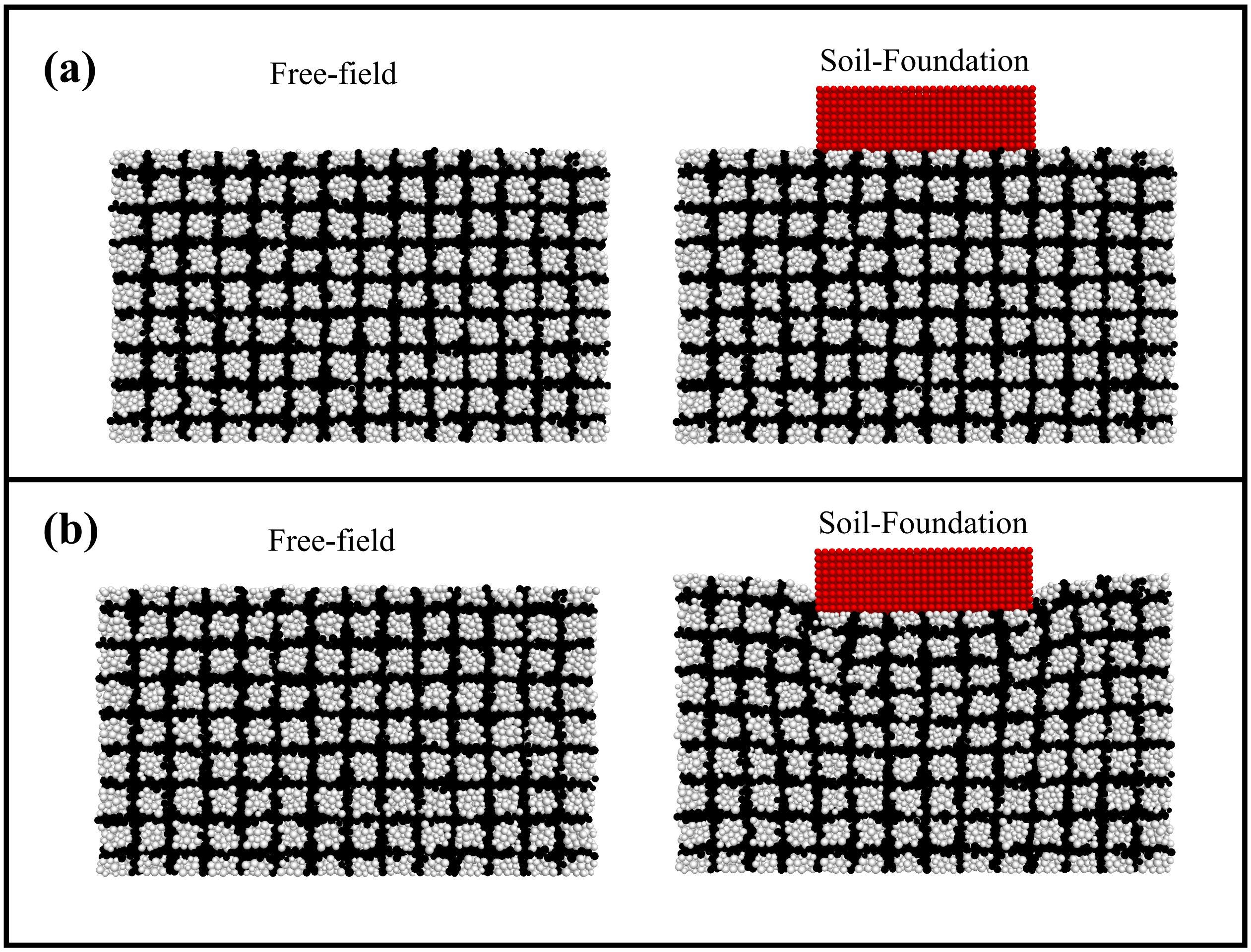

Figure 13: (a) Initial shape of the models, and (b) deformed shapes at the end of simulations

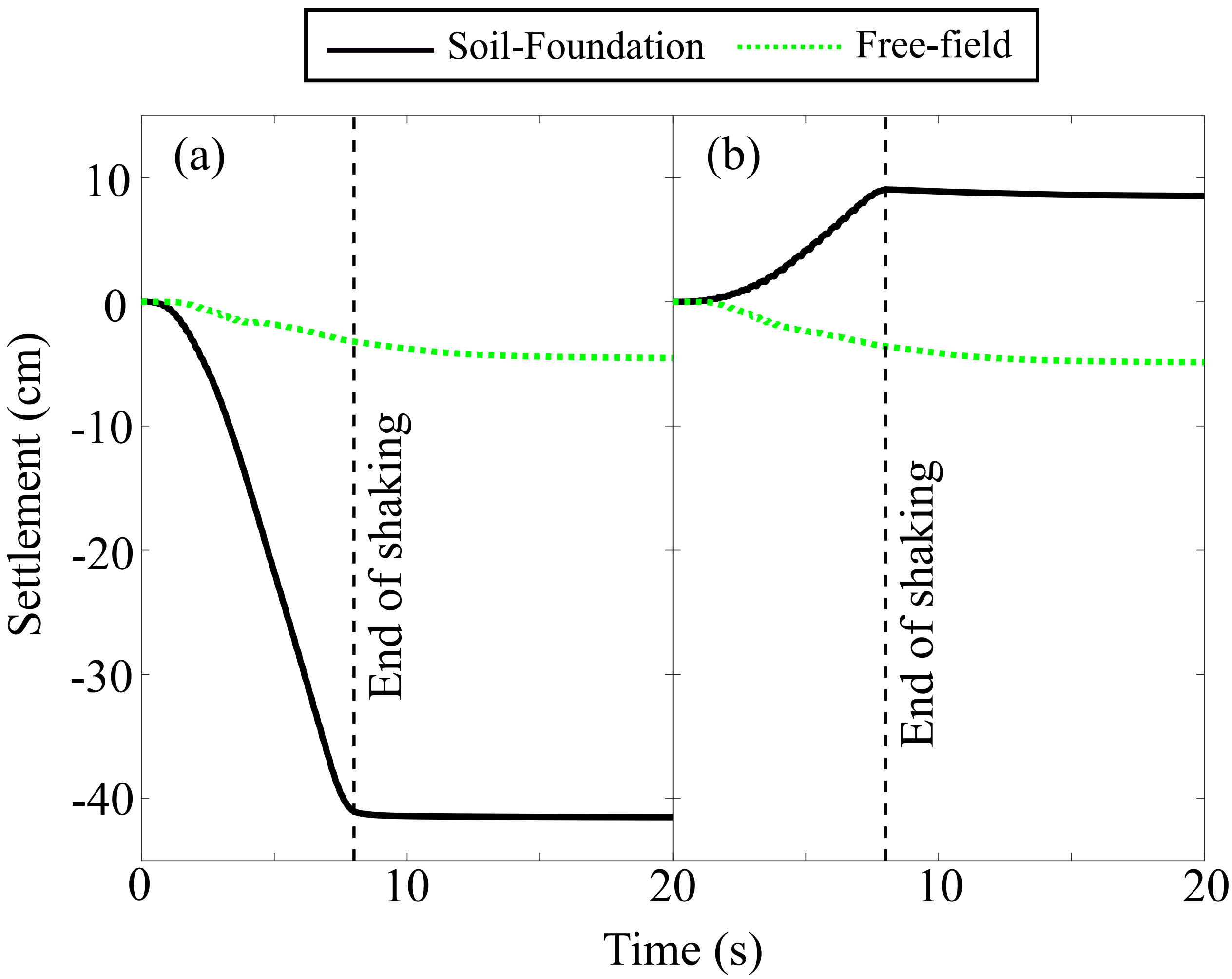

Figure 14: Time histories of ground settlement (a) at the models center, and (b) near the left boundary of the models

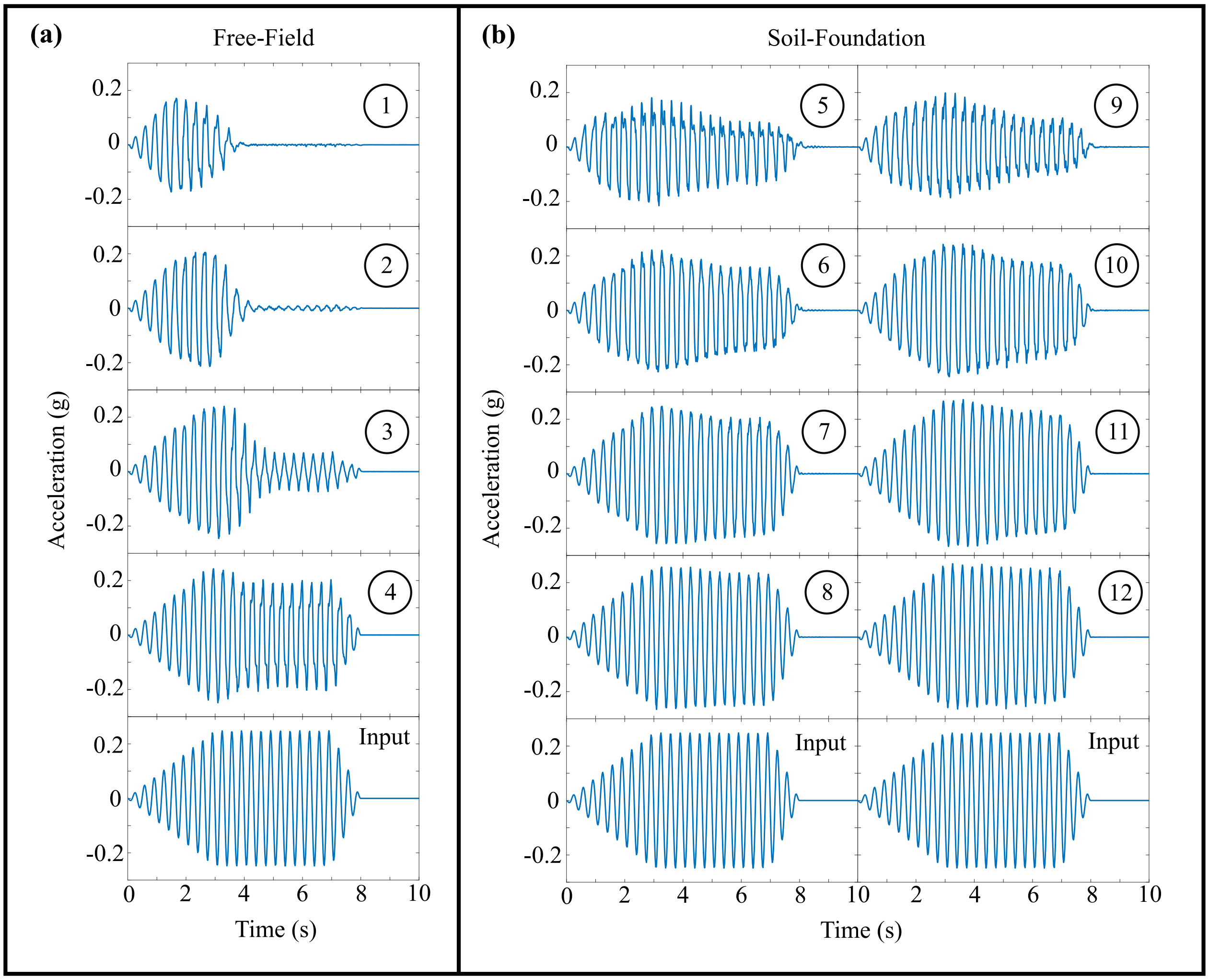

Figure 15: Time histories of average particle acceleration at different measurement locations inside (a) the free-field model, and (b) the soil-foundation system

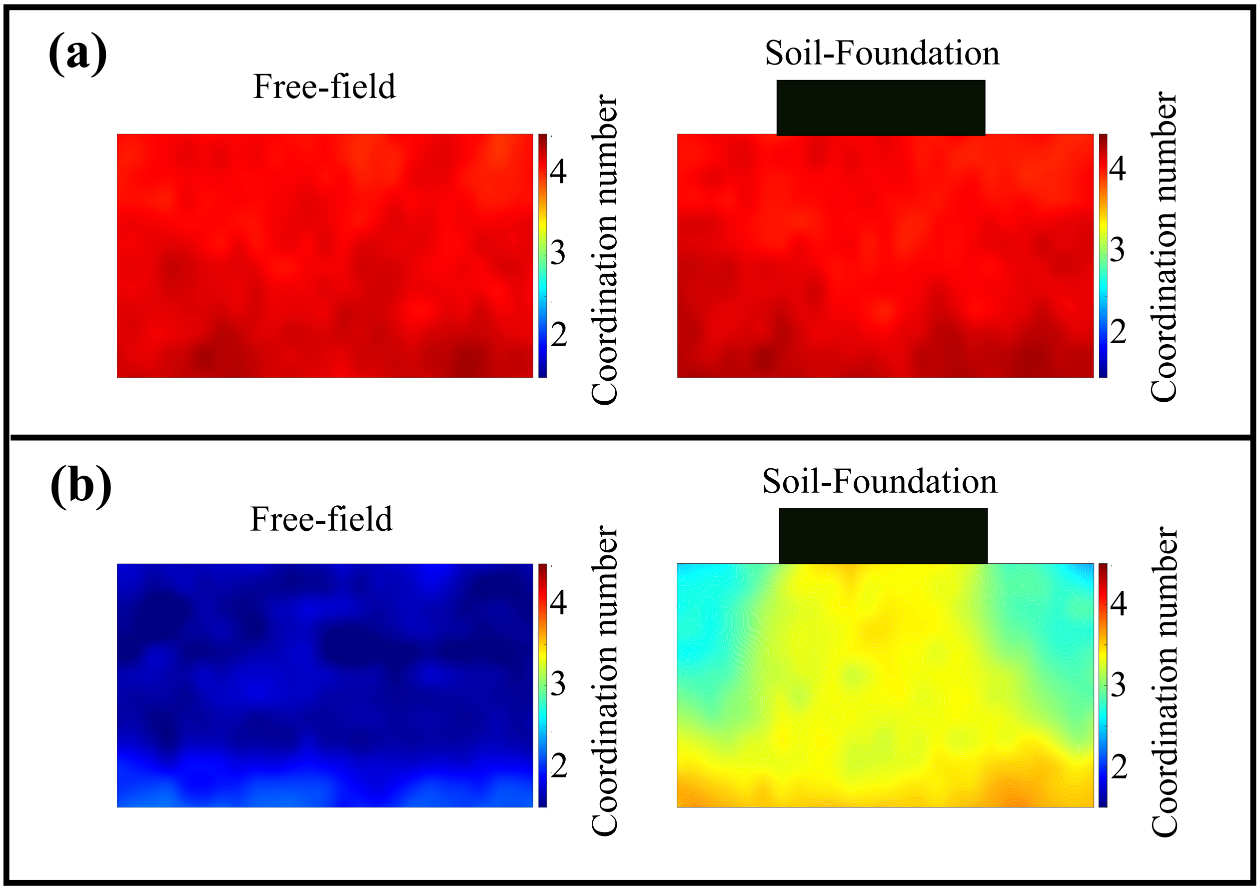

Figure 16: Contours of (a) initial coordination number, and (b) minimum coordination number reached during simulations

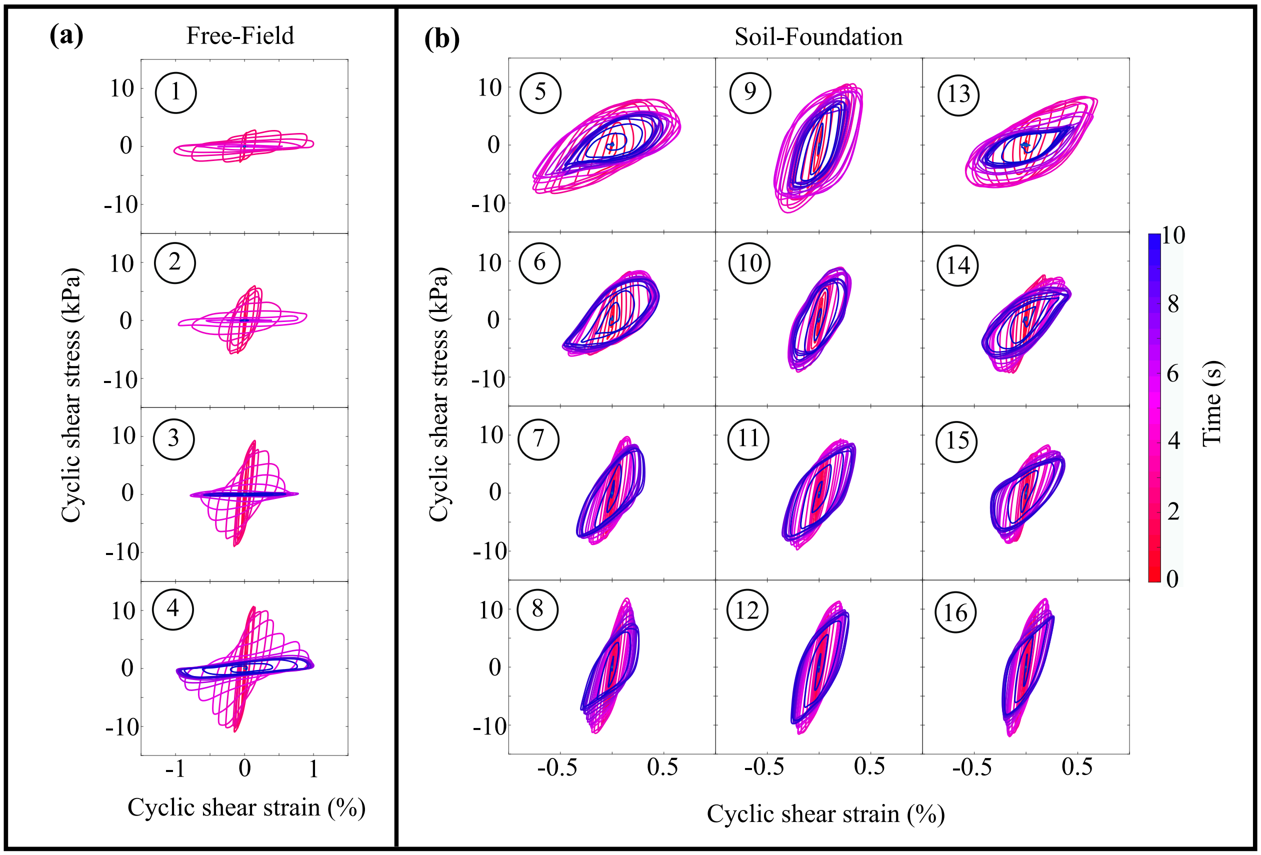

Figure 17: Cyclic shear stress-shear strain loops at different locations inside (a) the free-field model, and (b) the soil-foundation system

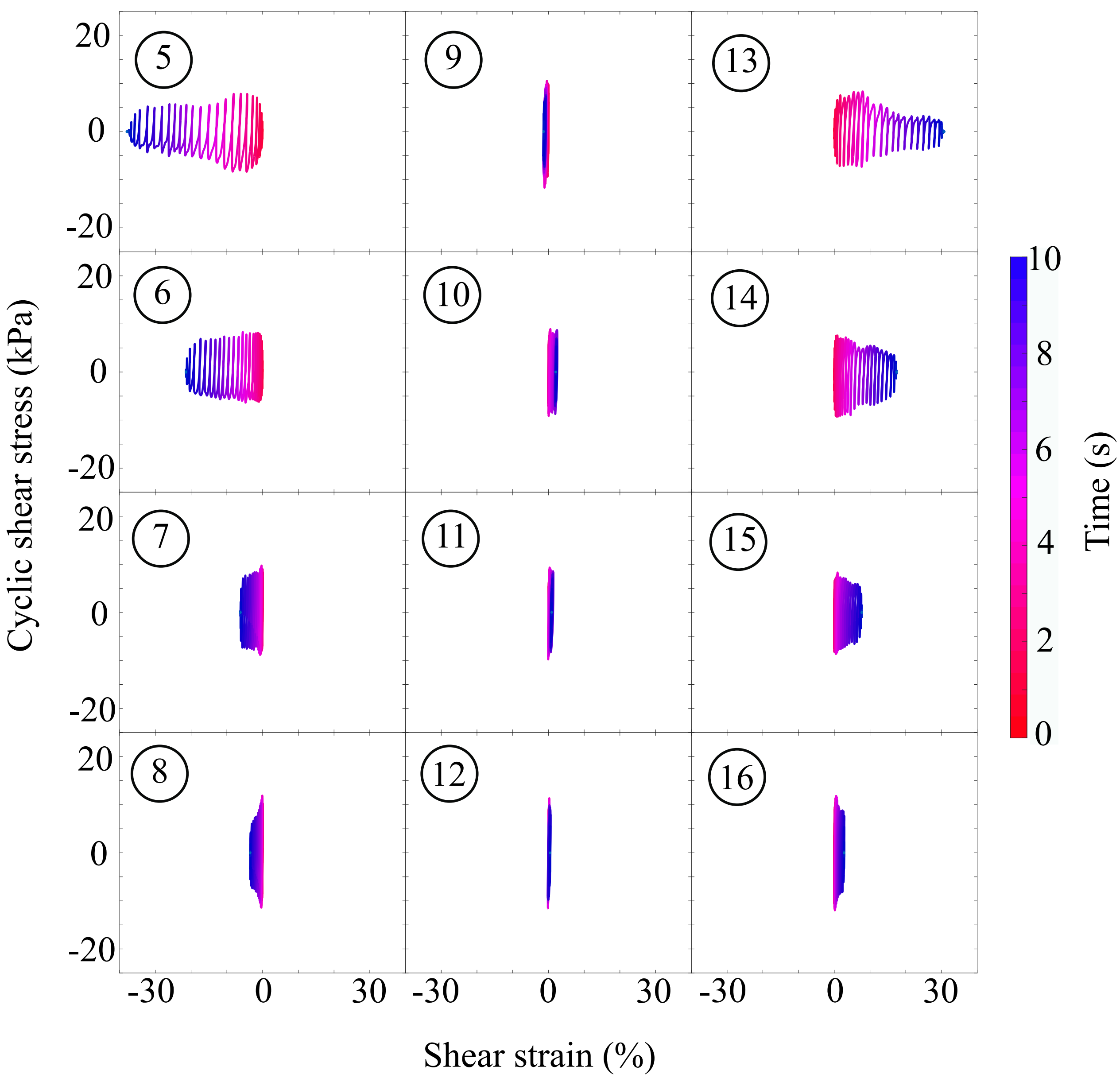

Figure 18: Plots of cyclic shear stress versus shear strain (non-cyclic) at different locations inside the soil-foundation system

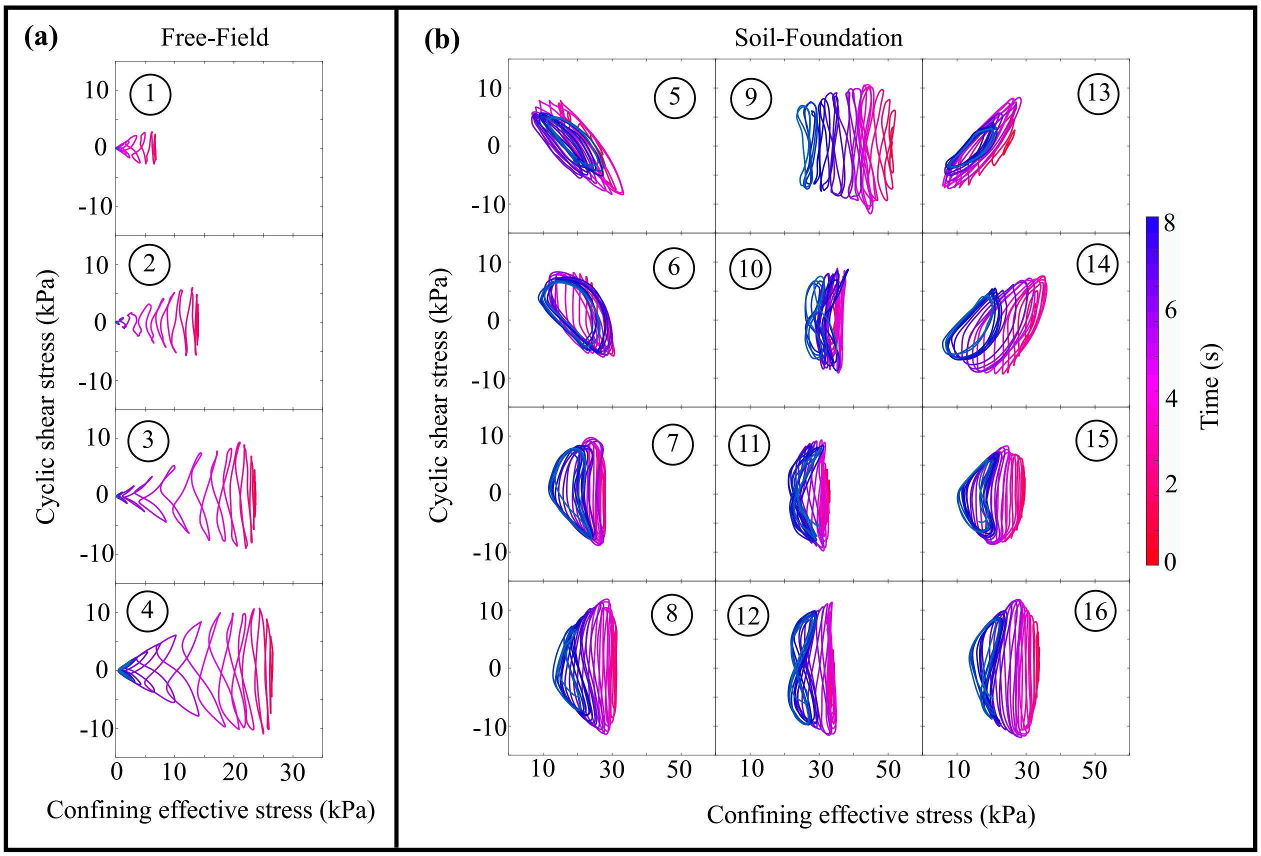

Figure 19: Time histories of effective stress path at different locations inside (a) the free-field model, and (b) the soil-foundation system

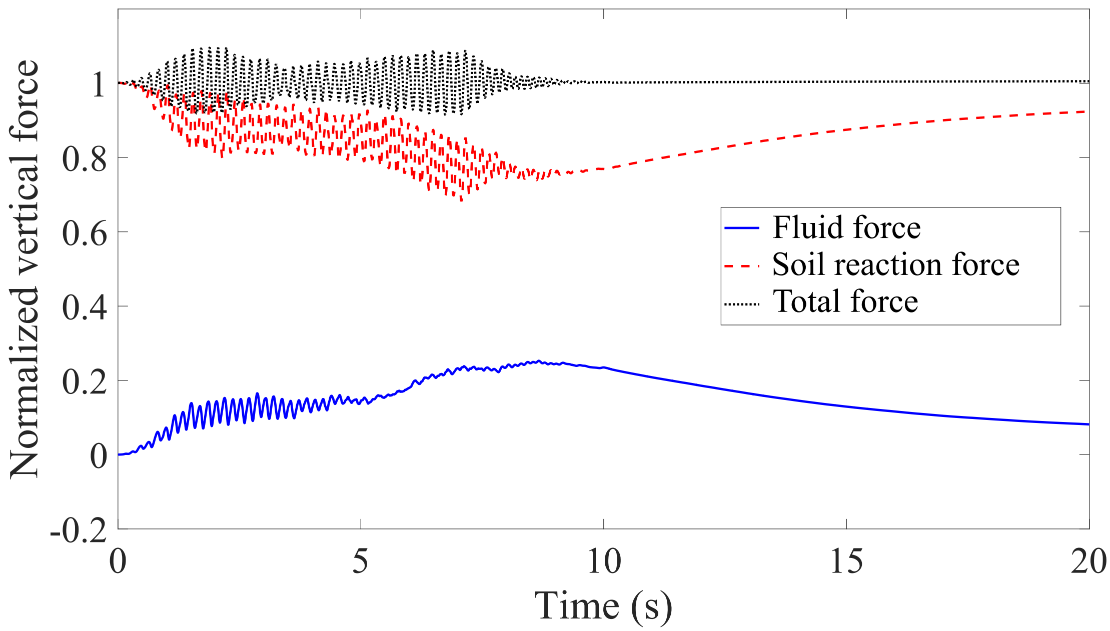

Figure 20: Time histories of vertical forces exerted on the foundation block normalized by its weight

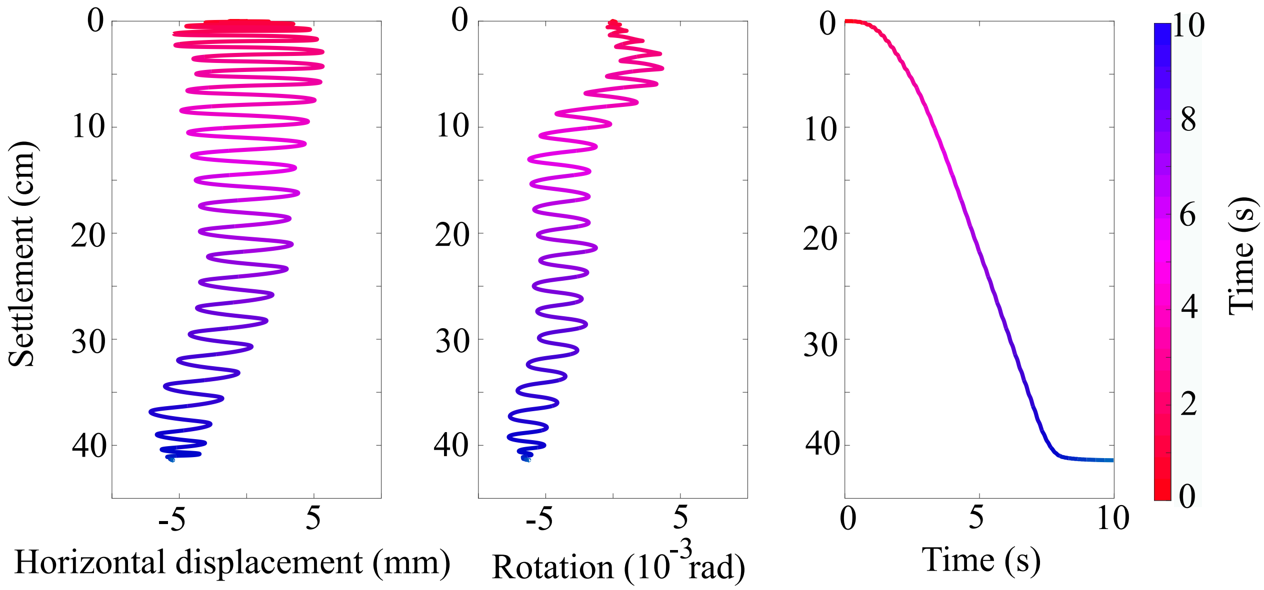

Figure 21: Plots of foundation settlement versus horizontal displacement, rotation and time

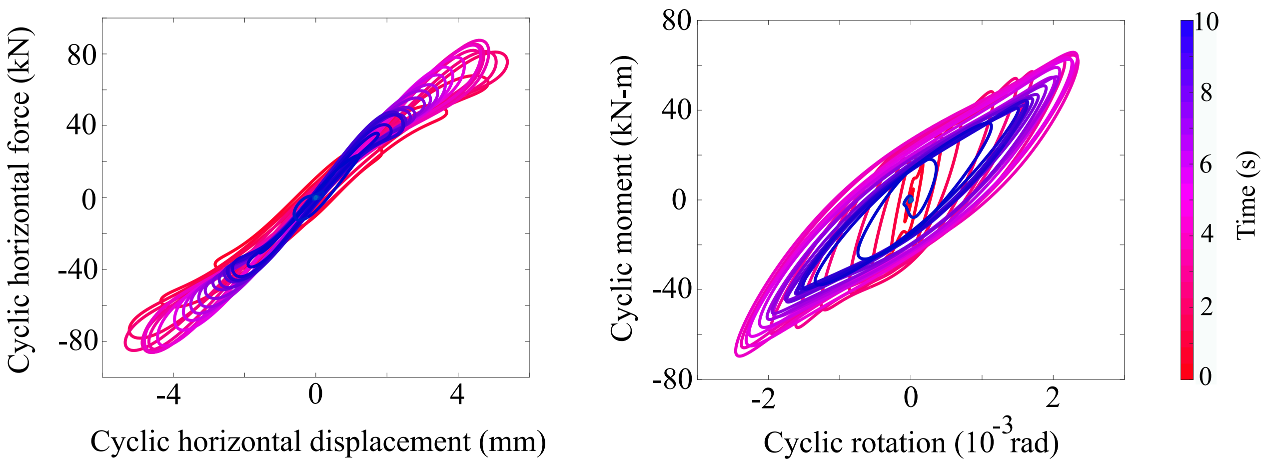

Figure 22: Plots of cyclic horizontal force-horizontal displacement and cyclic moment-rotation for the foundation block

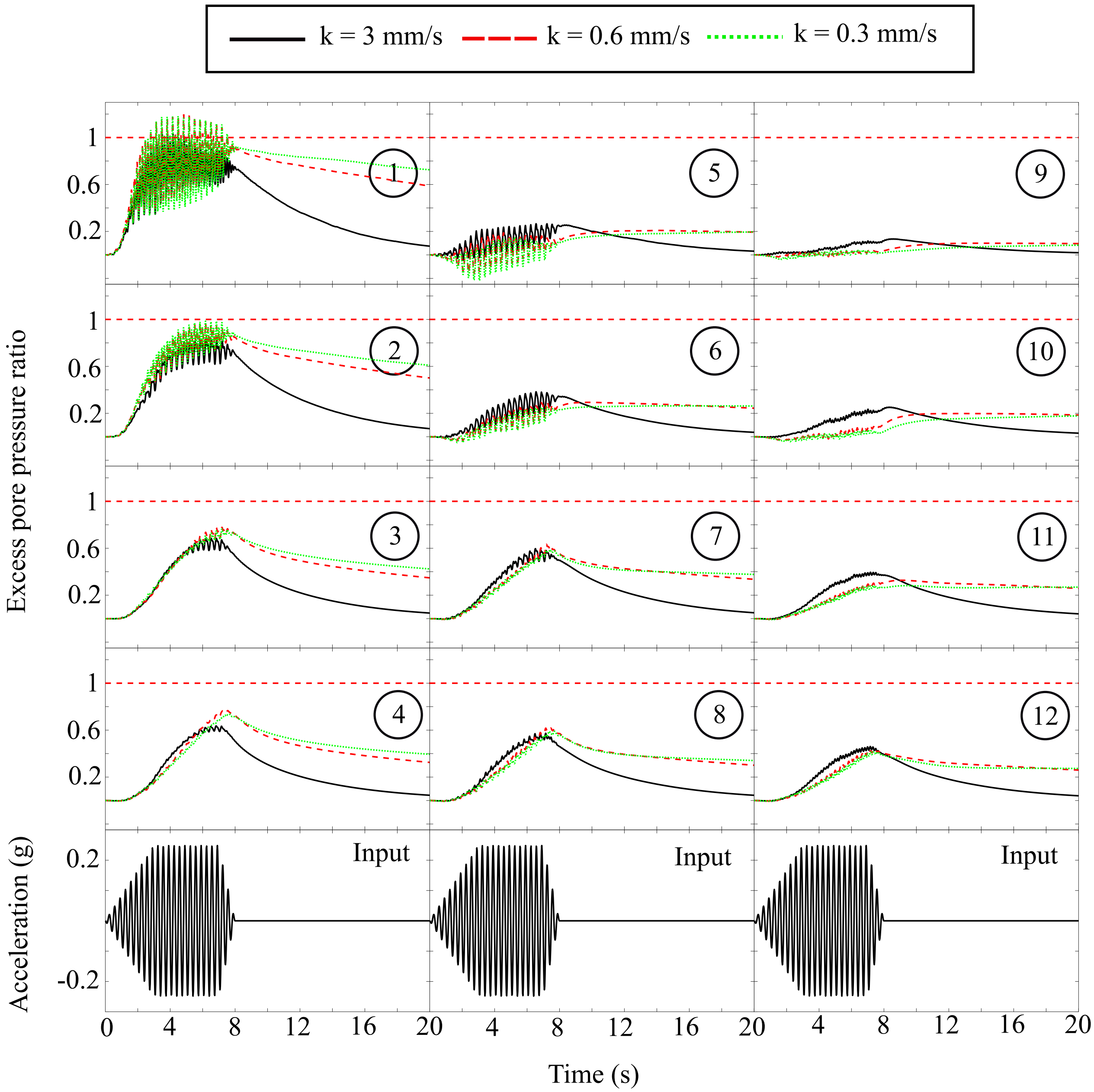

Figure 23: Time histories of excess pore pressure ratio at various measurement locations within the soil-foundation systems with different permeability coefficients

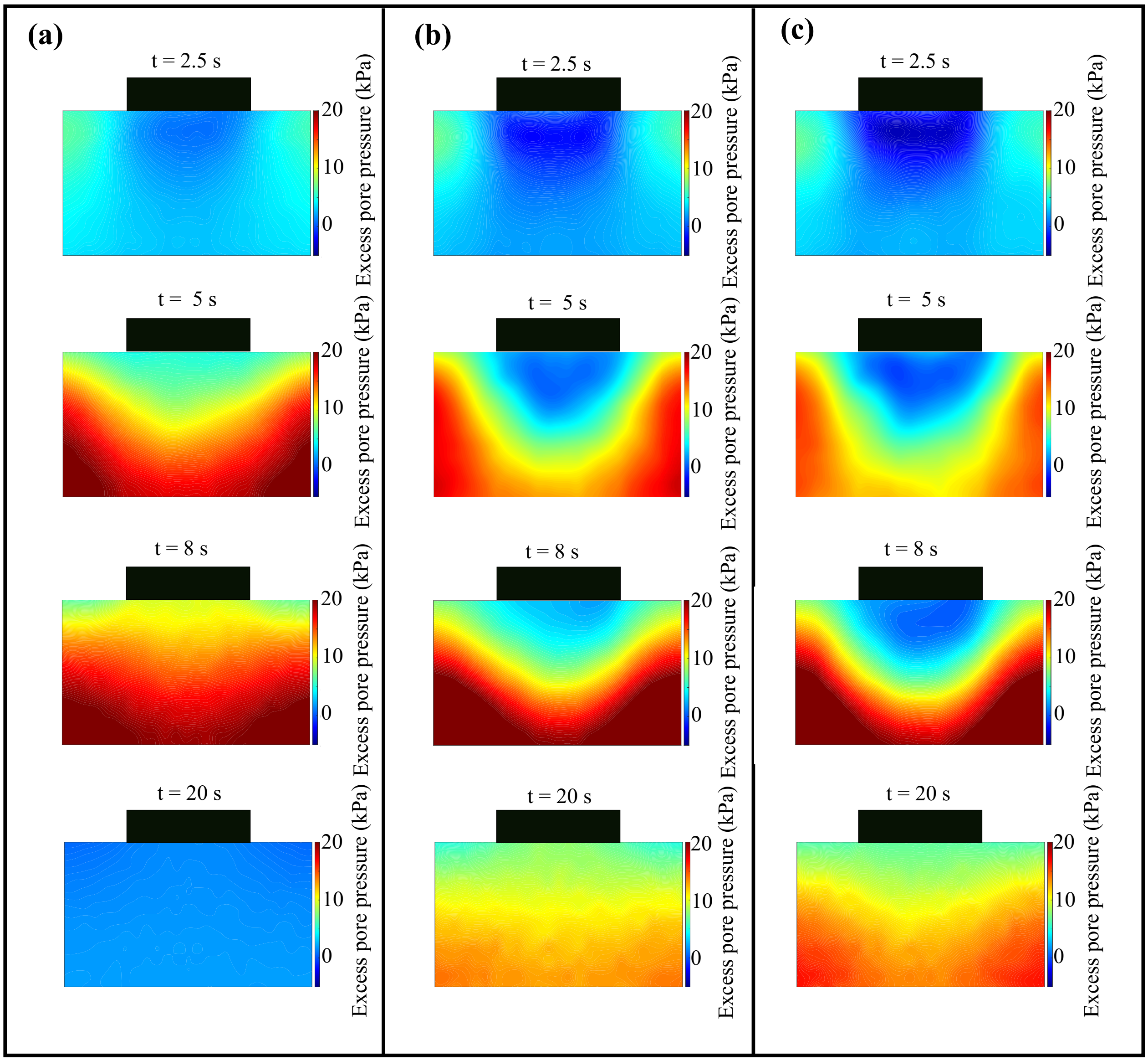

Figure 24: Contours of excess pore pressure at different moments in the deposits overlain by the foundation with permeability coefficients of (a) 3 mm/s, (b) 0.6 mm/s, and (c) 0.3 mm/s

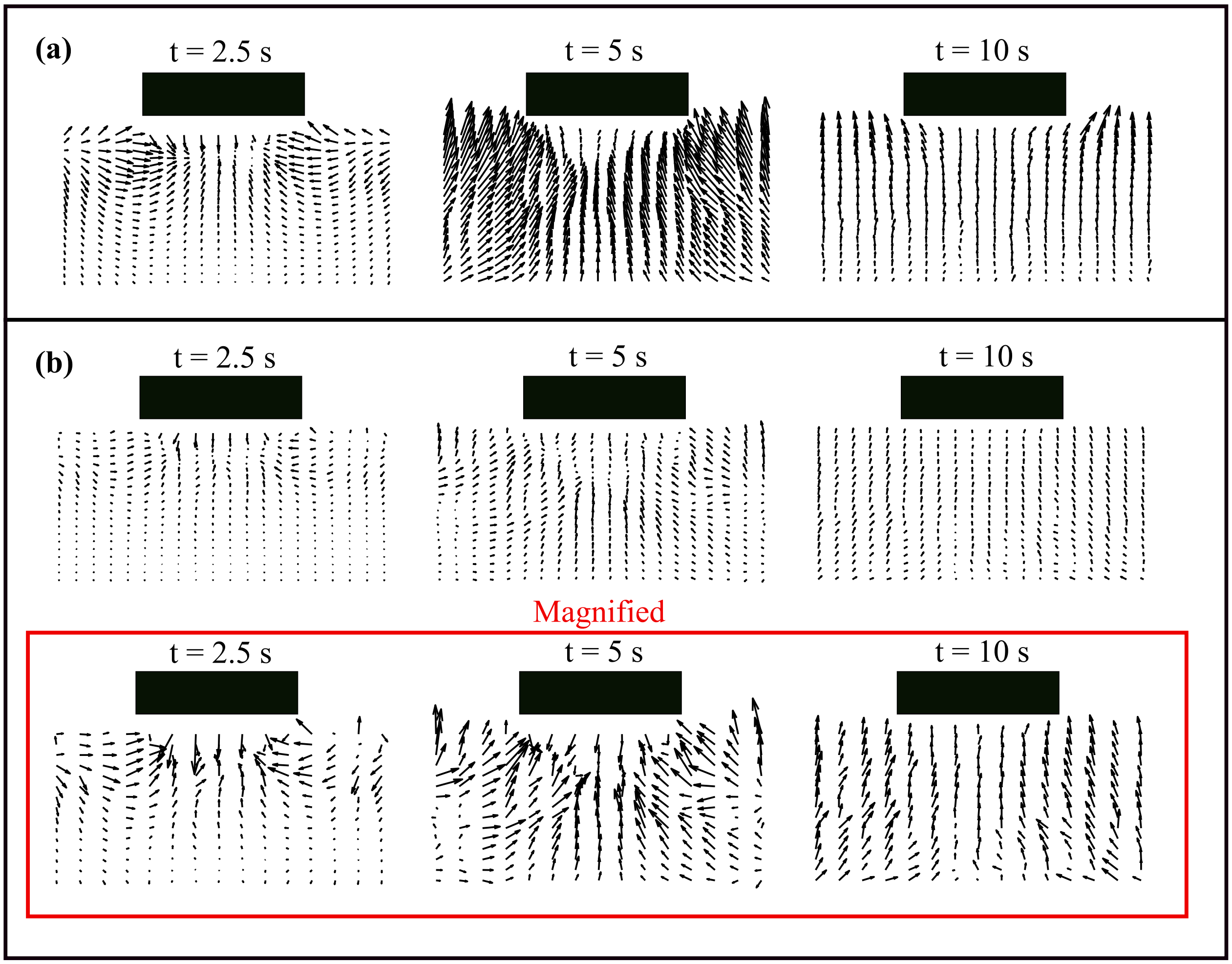

Figure 25: Vector fields of relative fluid velocity at different moments in the deposits overlain by the foundation with permeability coefficients of (a) 3 mm/s, and (b) 0.6 mm/s

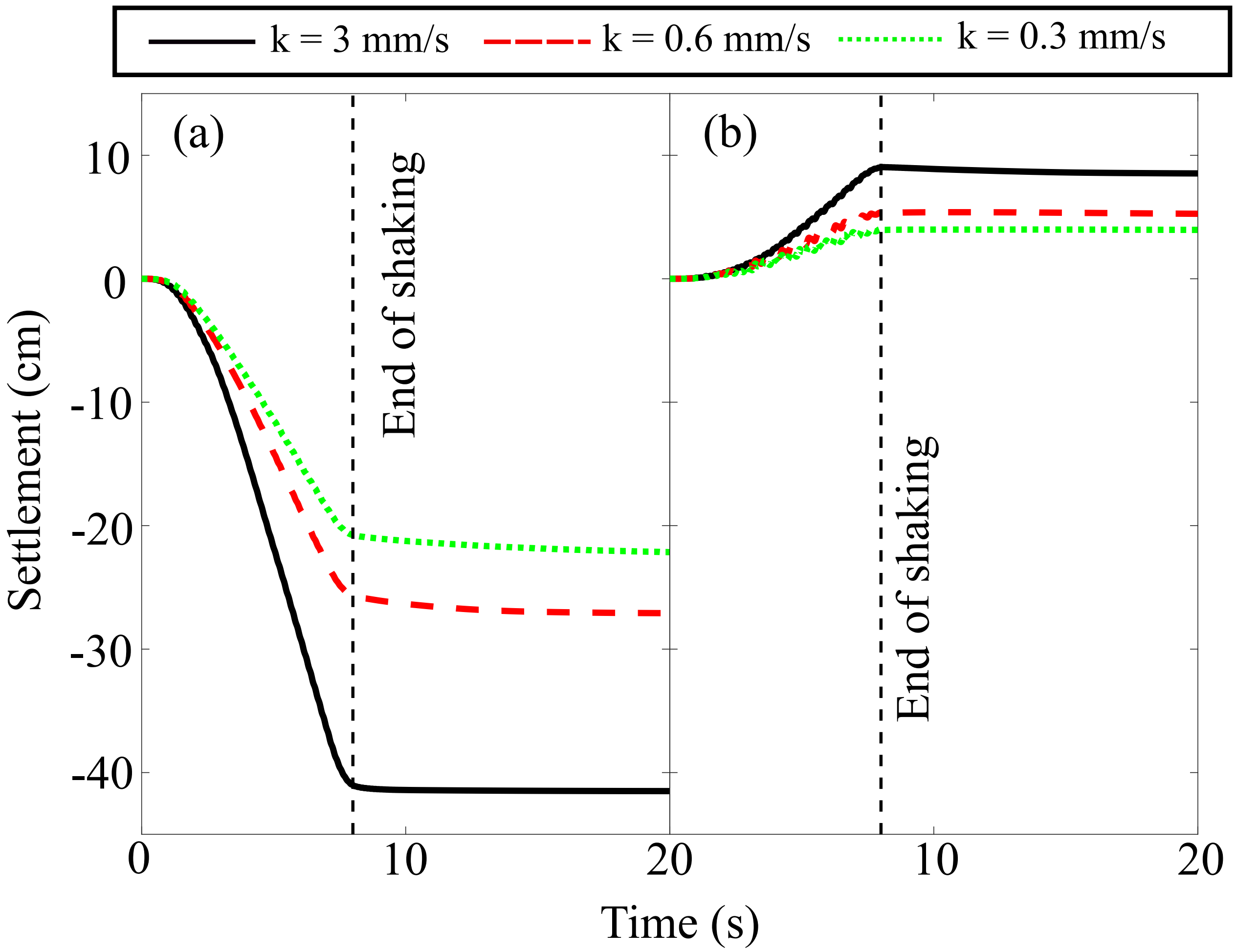

Figure 26: Time histories of ground settlement (a) at the models center, and (b) near the left boundary of the soil-foundation models with different permeability coefficients

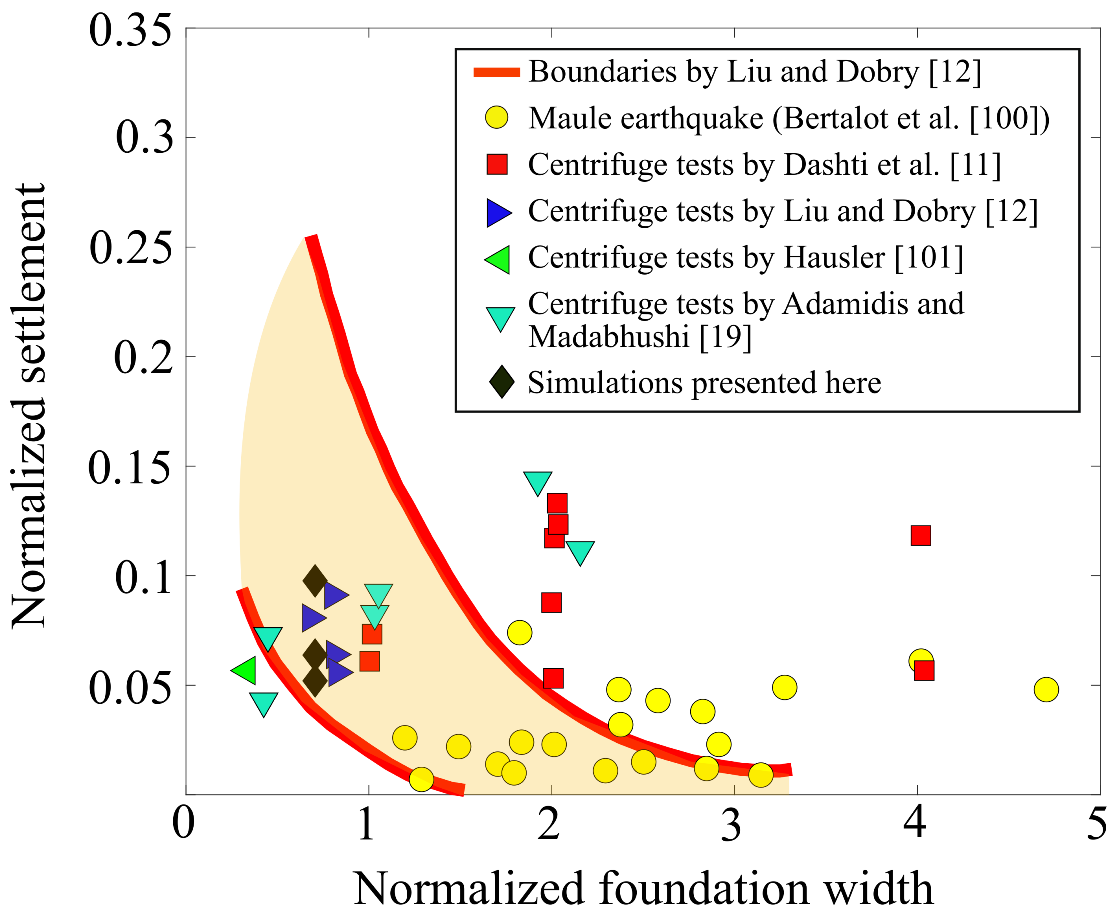

Figure 27: Foundation settlement versus foundation width, both normalized by the depth of liquefiable soil layer

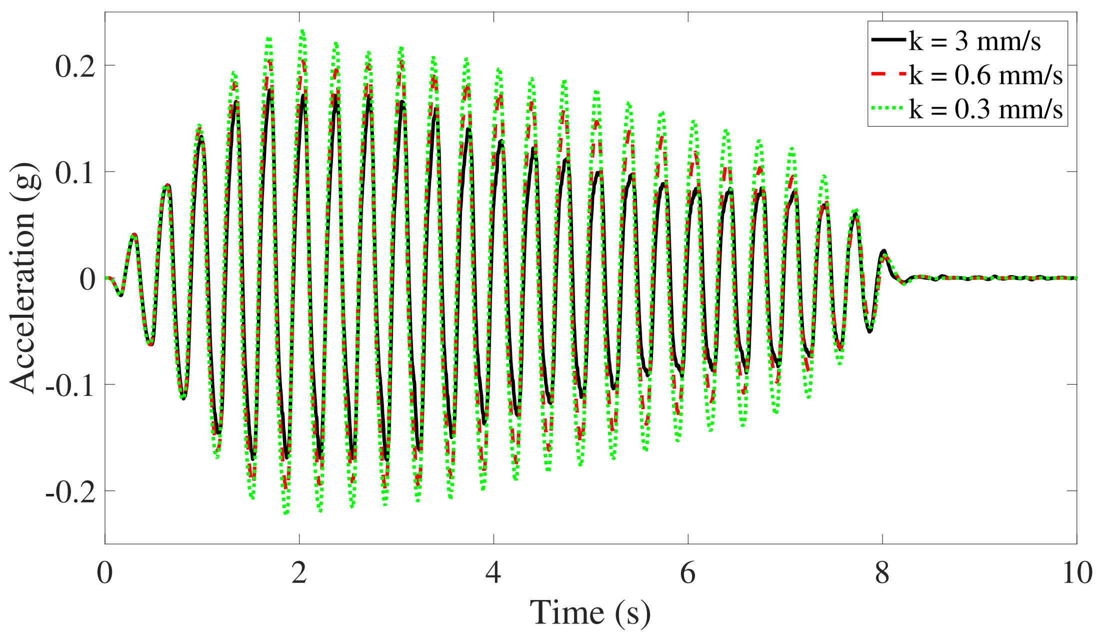

Figure 28: Time histories of foundation acceleration in the soil-foundation models with different permeability coefficients